Journal of Volcanology and Geothermal Research 442 (2023) 107898

Contents lists available at ScienceDirect

Journal of Volcanology and Geothermal Research

journal homepage: www.journals.elsevier.com/journal-of-volcanology-and-geothermal-research

Overview of seismo-acoustic tremor at Oldoinyo Lengai, Tanzania: Shallow storage and eruptions of carbonatite melt

Miriam Christina Reiss [a,b,*], Francesco Massimetti [c], Amani S. Laizer [d], Adele Campus [c], Georg Rümpker [a,e], Emmanuel O. Kazimoto [d]

[a] Institute of Geosciences, Goethe University Frankfurt, Frankfurt, Germany
[b] now at Institute of Geosciences, Johannes Gutenberg University Mainz, Mainz, Germany
[c] Department of Earth Sciences, University of Torino, Torino, Italy
[d] Department of Geology, University of Dar es Salaam, Dar es Salaam, Tanzania
[e] Frankfurt Institute for Advanced Studies, Frankfurt, Germany

ARTICLE INFO

Keywords:
Seismo-acoustic tremor
Harmonic tremor
Open-vent volcano
Carbonatite eruptions

ABSTRACT

We analyze volcanic tremor from Oldoinyo Lengai, Tanzania, which is currently the only active volcano on Earth producing carbonatitic lavas. Here, we use data from the recent SEISVOL deployment and focus on a co-located seismic and infrasound station about 200 m below the summit. We show the very first observations of seismo-acoustic tremor caused by carbonatitic eruptions. This seismo-acoustic tremor is highly variable throughout the ~one year of data which we characterize by analyzing its seismic amplitude, duration, recurrence, dominant seismic frequency and harmonics. Frequency gliding occurs frequently and over short (minutes to hours) to long time scales (hours to days) and likely reflects different time-dependent mechanisms, such as evenly-spaced repeating events with a change in inter-event times, crater dynamics that alter resonators, and dike intrusions. Seismic and acoustic wavefields correlate well for stronger eruptive sequences but are only partially coherent which suggests that high-frequency seismic tremor (up to 25 Hz) may be caused by the low viscosity of the carbonatitic melt and not by ground-coupled airwaves. In addition, the comparison between seismic-acoustic and satellite InfraRed thermal data allows us to infer different volcanic activity styles which partially alternate throughout the year: intrusive activity and the construction of hornitos, degassing, activity from a lava pond, and varying styles of extrusive activity, in particular spattering. Our study provides important insights into the eruption dynamics of this peculiar volcano which suggests shallow melt storage within the crater floor.

1. Introduction

The observation and analyses of seismic and acoustic data are one of the most commonly used tools in volcano monitoring and provide the basis of our understanding of magma transport and eruption processes (e.g. Matoza and Roman, 2022; McNutt, 1996). A signal commonly observed pre-, syn- and post-eruption is volcanic tremor, which is often defined as a long-lasting signal without clear onset or end in a frequency range below 5 Hz (e.g. McNutt, 1992). It thus likely plays a key role in characterizing the internal state of a volcano. However, a set of well-defined criteria for tremor is missing likely due to the variability of the observed tremor signals at different volcanoes, lack of data from a wide variety of volcanoes, and difficulties in localizing tremor due to the absence of clear onsets. Accordingly, attributing tremor to a common source process has thus far proven to be difficult. Common models for tremor include crack propagation (e.g. Aki et al., 1977; Chouet, 1983) and resonance of fluid flow in conduits (e.g. Chouet, 1988) while many different trigger mechanisms have been described, such as self-sustained oscillations, magmatic-hydrothermal interactions, magmatic degassing and brittle failure of melt (see Matoza and Roman, 2022; and references therein).

The ability to infer source processes largely depends on the type of data set available. Seismic and acoustic instruments provide complementary data of the signals often observed in the vicinity of volcanoes. While seismic data can elucidate subsurface processes such as earthquakes and tremor, and be used to infer the subsurface structure underneath volcanoes (e.g. Chouet and Matoza, 2013; Konstantinou and Schlindwein, 2002; Wilding et al., 2023; Koulakov and Shapiro, 2021),

* Corresponding author at: Institute of Geosciences, Johannes Gutenberg University Mainz, Mainz, Germany.
E-mail address: miriam.reiss@uni-mainz.de (M.C. Reiss).

https://doi.org/10.1016/j.jvolgeores.2023.107898
Received 26 June 2023; Received in revised form 22 August 2023; Accepted 27 August 2023
Available online 1 September 2023

acoustic data can help to detect surficial processes such as explosions and degassing (e.g. Johnson and Ripepe, 2011; Fee and Matoza, 2013). Recent advances have focused on analyzing the coupling of seismic and acoustic wavefields in volcanic tremor to better characterize source processes (e.g. Matoza and Fee, 2014; McKee et al., 2018; Ichihara et al., 2021). If available, ground-based degassing measurements can help to further pin down source mechanisms (e.g. Fischer et al., 1994).

Satellite-based data can add significantly to our understanding of eruptive processes and how they relate to geophysical data, particularly in the absence of other ground-based observations providing homogeneous and long-term measurements of volcanic activity, which are essential to establish background levels of activity and enhance the understanding of volcanic processes (Reath et al., 2019; Coppola et al., 2020). Thermal anomalies can be recorded by a variety of satellite sensors with InfraRed capabilities (IR, measurement within the 0.7 to 20 μm waveband; Harris, 2013), such as the Moderate Resolution Imaging Spectroradiometer (MODIS) or MultiSpectral Instrument (MSI; Coppola et al., 2016; Massimetti et al., 2020). They can be used to detect anomalous volcanic temperatures, and more significantly their variation in space and time, and to retrieve fundamental parameters such lava flow dimensions, location, effusive rates and erupted volumes (Oppenheimer et al., 1993; Harris, 2013; Coppola et al., 2022).

Many authors have suggested that the amplitude of volcanic tremor and effusion rates are linked, particularly in volcanoes with dominant effusive behavior (e.g. Aki and Koyanagi, 1981; Battaglia et al., 2005; Coppola et al., 2009). If the mass of the moving magma is proportional to the dissipated energy, the relationship between effusion rate and tremor is quadratic (Battaglia et al., 2005) while it should be linear if the tremor is related to the degassing of ascending magma if the amount of gas is proportional to the flux of magma and the bubble collapse rate is constant (Coppola et al., 2009 and reference therein). Eibl et al. (2017) show that caution must be excised when using seismic amplitudes or energy to estimate eruptive volumes in the presence of more than one tremor source.

Thus far, there are no published records of tremor at Oldoinyo Lengai volcano. Seismicity studies are available for part of the 2007 eruption (Calais et al., 2008) and for the Natron Rift (Albaric et al., 2010, 2014; Weinstein et al., 2017; Oliva et al., 2019, Reiss et al., 2021). While Roecker et al. (2017) image the crustal structure of the North Tanzanian Divergence, more detailed imaging is available for the plumbing system of Oldoinyo Lengai itself (Reiss et al., 2022). There is no permanent seismic, acoustic or gas monitoring, but the TZVOLCANO network (Stamps et al., 2016) consists of seven Global Navigation Satellite System (GNSS) stations used to detect volcanic deformation (Daud et al., 2023).

Here, we present an analysis of approximately one year of seismo-acoustic tremor data from Oldoinyo Lengai volcano, Tanzania, from the recent SEISVOL deployment (Seismic and Infrasound networks to study the volcano Oldoinyo Lengai; Reiss and Rümpker, 2020). We use data from a co-located seismic and infrasound station about 200 m below the summit and a variety of tools to characterize the seismo-acoustic tremor, which are the very first recordings of tremor caused by carbonatitic melt. We focus on analyzing the frequency content (i.e. dominant and harmonic frequencies, and changes thereof, frequency gliding), a tremor detector for banded, recurring tremor signals, correlation and coherency analysis between seismic and infrasound data and support our analysis with satellite-based thermal measurements.

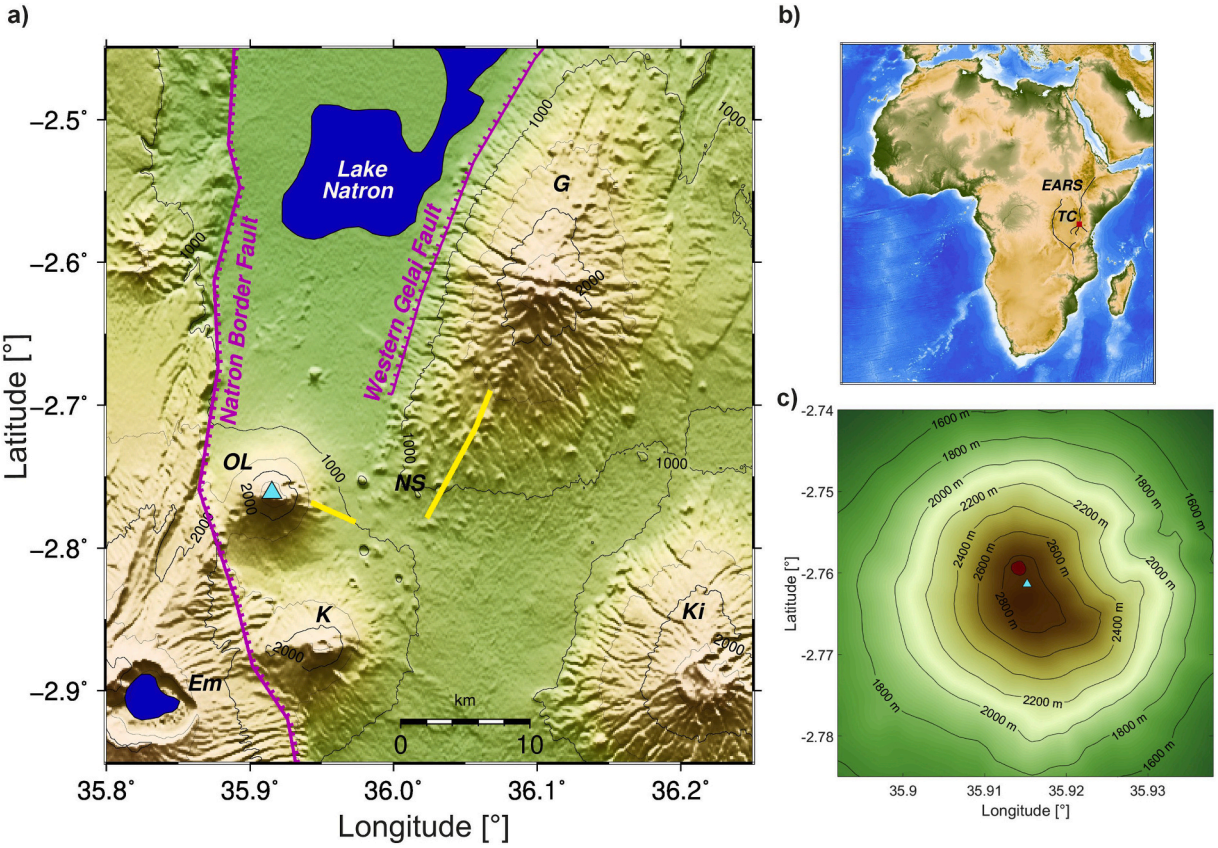

Fig. 1. Map of the tectonic setting. a) Natron basin with volcanoes Gelai (G), Oldoinyo Lengai (OL), Naibor Soito (NS), Kerimasi (K), Ketumbeine (Ki) and Emgbai (Em). Yellow lines are 2007 dike intrusions, magenta lines are major fault zones. Cyan triangle indicates the location of the seismic and acoustic sensors. b) Larger tectonic setting within the East African Rift System (EARS) shown by solid black lines which frames the Tanzania Craton (TC). Red square indicates the location of the Natron basin. c) Zoom into Oldoinyo Volcano. The currently active crater is shaded as dark red area and the position of co-located seismic and infrasound station is highlighted with a cyan colored triangle. (For interpretation of the references to color in this figure legend, the reader is referred to the web version of this article.)

2. Volcano-tectonic setting

Oldoinyo Lengai is located in the Natron Basin of the North Tanzanian Divergence, which itself is part of the longest continental rift worldwide, the East African Rift System (EARS, Fig. 1a,b). Magmatism in the North Tanzanian Divergence initiated at ~6 Ma forming the 200 km-wide diachronous Ngorongoro-Kilimanjaro Volcanic Belt which consists of a large number of basaltic shields and composite cones (Le Gall et al., 2008; Mana et al., 2015; Muirhead et al., 2015, Fig. 1). Considering the wide spectrum of lava compositions and high CO_2 content, these are likely sourced from an enriched metasomatized mantle (Dawson, 1992; Foley et al., 2012; Mollex et al., 2018; Muirhead et al., 2020, Fischer et al., 2009; Mana et al., 2015).

Oldoinyo Lengai is situated at the southern end of the Natron basin and adjacent to its western border fault. In its immediate vicinity is Naibor Soito volcanic field, a monogenetic cone field which is located on the southern flanks of the ~1 Ma old Gelai volcano (Mana et al., 2015; Muirhead et al., 2016; Fig. 1a). Eruptions at Oldoinyo Lengai initiated ~0.37 Ma ago (e.g. Dawson et al., 1995; Sherrod et al., 2013) and are known for alternating between large explosive eruptions and small-scale effusive eruptions. Recent explosive volcanism occurred in 1917, 1940–1941, 1966–1967 and 2007–2008, and generally involved nephelinitic silicate magma (Dawson et al., 1995; Klaudius and Keller, 2006; Keller et al., 2010). Additionally, Oldoinyo Lengai volcano is unique due to its production of natrocarbonatite lava with extremely low viscosity (10^{-1} to 10^{2} Pa s) and low temperature (~490–590 °C) (e.g. Krafft and Keller, 1989; Fischer et al., 2009).

The 2007–2008 explosive period of Oldoinyo Lengai was preceded and accompanied by a July–September 2007 earthquake swarm (70 earthquakes with $M > 4$) associated with a dike intrusion below Naibor Soito volcanic field (Baer et al., 2008; Calais et al., 2008; Biggs et al., 2009; Biggs et al., 2013; Kervyn et al., 2010). InSAR data also support a second diking event 3.4 km below Oldoinyo Lengai between October and December 2007 (Biggs et al., 2013). Both events were thought to be accompanied by the emptying of a shallow magmatic reservoir in close proximity as inferred from InSAR data (Calais et al., 2008; Biggs et al., 2009; Biggs et. 2013). This was most likely driven by a pressurized deep magma chamber, and magma was then distributed from there in the shallow crust, and fed into the Oldoinyo Lengai chamber according to the local background stress (Biggs et al., 2013; Baer et al., 2008).

New constraints on the plumbing system of the Natron basin arise from several new seismological studies. Roecker et al. (2017) imaged a low velocity, high Vp/Vs area by using the seismicity catalog of Weinstein et al. (2017) and interpreted it as a single magma chamber between both volcanoes below a depth of 15 km. These data sets imaged two elliptical zones of low velocity and high seismicity which were interpreted as sills that might have fed the 2007 dike intrusion, and triggered the eruption at Oldoinyo Lengai (Oliva et al., 2019). Using data from the SEISVOL project, Reiss et al. (2021 & 2022) were able to show a detailed 3D image of a complex volcanic plumbing system. Seismicity patterns show lateral and vertical connections between shallow- and deep-seated melt bodies, where fluid and melt transport to the surface is facilitated by intrusion of dikes and sills (Reiss et al., 2021). Absorption imaging revealed a melt body at 8–12 km depth wedged between the two high seismicity zones (Reiss et al., 2022) which likely represents a silicate magma reservoir. Scattering and absorption patterns further suggest a highly fractured fluid-filled Natron border fault which may enhance the transport and production of carbonatite melts. Daud et al. (2023) used GNSS and InSAR data to derive a deflating shallow source off-set from the volcano at ~3.5 km depth between 2016 and 2021, suggesting that melt is transferred from the crust to shallower parts of the volcanic system.

In the past, thermal emissions from the summit crater of Oldoinyo Lengai are sourced either by fumaroles, small open cracks or vents, lava ponds, or cooling lava from small pools, flows or spatter, which were small in terms of size, volume and eruption rate compared the onset of the explosive eruption in September 2007 (Vaughan et al., 2008; Kervyn et al., 2010). Following a period of quiescence after the last explosive eruption in 2007–2008, thermal data shows increased sporadic but ongoing thermal activity since late 2018 (see S1). This is supported by eye-witnesses of effusive eruptions and degassing, as well as satellite imagery detailed by the Global Volcanism Program (GVP, 2019). In 2019, the crater was about 300 m wide and 70 m deep, and sits below the now inactive south crater which is the highest elevation of this volcano (GVP, 2019; Fig. 1c).

3. Data and methods

We use data from the recent SEISVOL deployment (Reiss and Rümpker, 2020). To characterize the volcanic tremor, we focus on a co-located seismic and infrasound station at 2845 m altitude, in a distance of about 200 m from erupting centers within the crater (Fig. 1c). We limit our analysis to these stations as the eruption signals were quite weak and, unperturbed by local seismicity, most strongly and continuously recorded on the seismic crater station while acoustic tremor was only recorded at the crater. Accordingly, we aim to provide an overview of the recorded wavefields in the vicinity of the crater to understand seismo-acoustic tremor. Both stations are digitized by a DiGOS datalogger; the seismic sensor is a three component, 4.5 Hz geophone sampled at 100 Hz. Accordingly, the instrument response function rolls off below its' natural frequency at 4.5 Hz which means that frequencies below 4.5 Hz are not well recorded. We only use the vertical component of this instrument. The infrasound sensor is an MB2018 from ISTerre sampled at 50 Hz. These sensors use small micromachined differential pressure transducer and provide a flat frequency response between 0.01 and 40 Hz. We remove both instruments' responses for all analyses and apply a bandpass filter, usually between 0.1 and 20 Hz or as specified.

3.1. Standard processing techniques

We employ several time series analyses tools to study strength, duration, frequency content and changes of the seismic and acoustic data. On seismic data, we first apply real-time seismic amplitude measurement, which is a measure of the average seismic amplitude in a given time interval (RSAM, Endo and Murray, 1991), to detect episodes of seismic tremor and estimate their relative strength. We use the standard window length of 60 s to calculate RSAM. Secondly, we calculate periodograms using the Fast Fourier Transform for hour-long seismic time windows and note the frequency with the highest power spectral density which we call 'dominant frequency' from here on. Thirdly, we apply a detector for harmonic tremor which is based on pitch-detection (Roman, 2017). This allows to detect the fundamental frequency of a continuous signal based on the harmonic power spectrum. The relationship between the peaks of this spectrum and the 'noise' level between them -also termed 'harmonic strength index' (HSI) - is used to estimate whether strong harmonics are present. As a detection threshold, we allow a minimum fundamental frequency of 0.1 Hz and an HSI of 10 which represents a moderately strict criterion on the definition of what constitutes harmonic tremor.

To estimate the relationship between seismic and infrasound data, we apply simple cross-correlation analysis (a similar analysis is performed by i.e. Cannata et al., 2013 or Barrière et al., 2018). We use hourly data files from both the seismic and infrasound station, apply a bandpass filter of 1-10 Hz and then cross-correlate the time series. We build daily stacks from March 1st 2019 until 17th November 2019 (when the infrasound stopped working). This allows us to analyze whether seismic and acoustic time series are generated by the same source process, in which case we would except a delay of the infrasound compared to the seismic trace given the different wave speeds in rock vs. air or whether seismic tremor is dominantly a ground-coupled airwave.

We further test the coherency of seismic and infrasound signals in the frequency domain after Matoza and Fee (2014) who focus on separating

air-ground and ground-air elastic wave coupling. The analysis is based on using the cross-spectrum between seismic and infrasound data to calculate which parts of the eruption tremor recorded on the seismogram are coherent with the infrasound signal. Accordingly, this method gives an estimate of which part of the tremor recorded on the seismogram can be attributed to wave propagation in rock versus wave propagation in air which couples back into the ground or wave propagation in rock and air. We use their approach to check if part of the tremor recorded on the seismic station is in fact caused by ground-coupled air waves.

3.2. Banded tremor detector

We develop a simple detector for banded seismic tremor episodes, i.e. where repeating, minutes-long tremor signals appear over hours to days, which often occur at Oldoinyo Lengai. The detector is based on significant changes of the energy in the spectrogram. For each hour-long seismic window (see Fig. 2a for an example trace), we first calculate a short-term average/long-term average (STA/LTA) using 1 s and 60 s respectively. If any value of STA/LTA function exceeds a threshold of 2.5 (also called trigger), we proceed assuming that a signal of interest occurred. We calculate a spectrogram using the fast Fourier transform assuming two thirds overlapping time windows of 10 s. Then, we apply a statistical change point approach to find points in time (Picard, 1985) with a significant change in the mean of the spectrum, which allows to detect seismic tremor onsets even if the signal-to-noise ratio in the time domain is unfavorable. The accuracy of the change points is restricted by the resolution of the spectrogram and is on the order of seconds. It is thus rather a detector than an exact picker but nevertheless allows to quantitively describe episodes of recurring seismic tremor signals since these are on the order of minutes.

A segment between change points is then accepted as banded tremor signal if the mean energy of the segment is larger than the mean energy of the entire hour (Fig. 2a). Teleseismic and regional earthquakes are easily detected and automatically filtered out based on the fact that they are usually captured by two or three short time segments with dominant low frequency energy and high amplitudes. Local earthquakes are also easily detected and removed based on their extremely high amplitudes compared to the average seismic tremor amplitude and extremely short duration. To focus on episodes where banded tremor occurs frequently, we only report those instances where banded tremor appears over a minimum of at least three time within one hour.

If a seismic tremor is detected, we apply the same change point analysis on the infrasound spectrogram(Fig. 2b). An independent detector of infrasound tremors based on STA/LTA is extremely difficult to establish due to high wind noise conditions and only works well for a short time period where wind is mostly absent. Accordingly, we omit this in favor of an overall stable detection of simultaneous seismic-acoustic tremors. If we detect a banded seismic tremor in a one hour-long window, we also check the corresponding infrasound trace. We

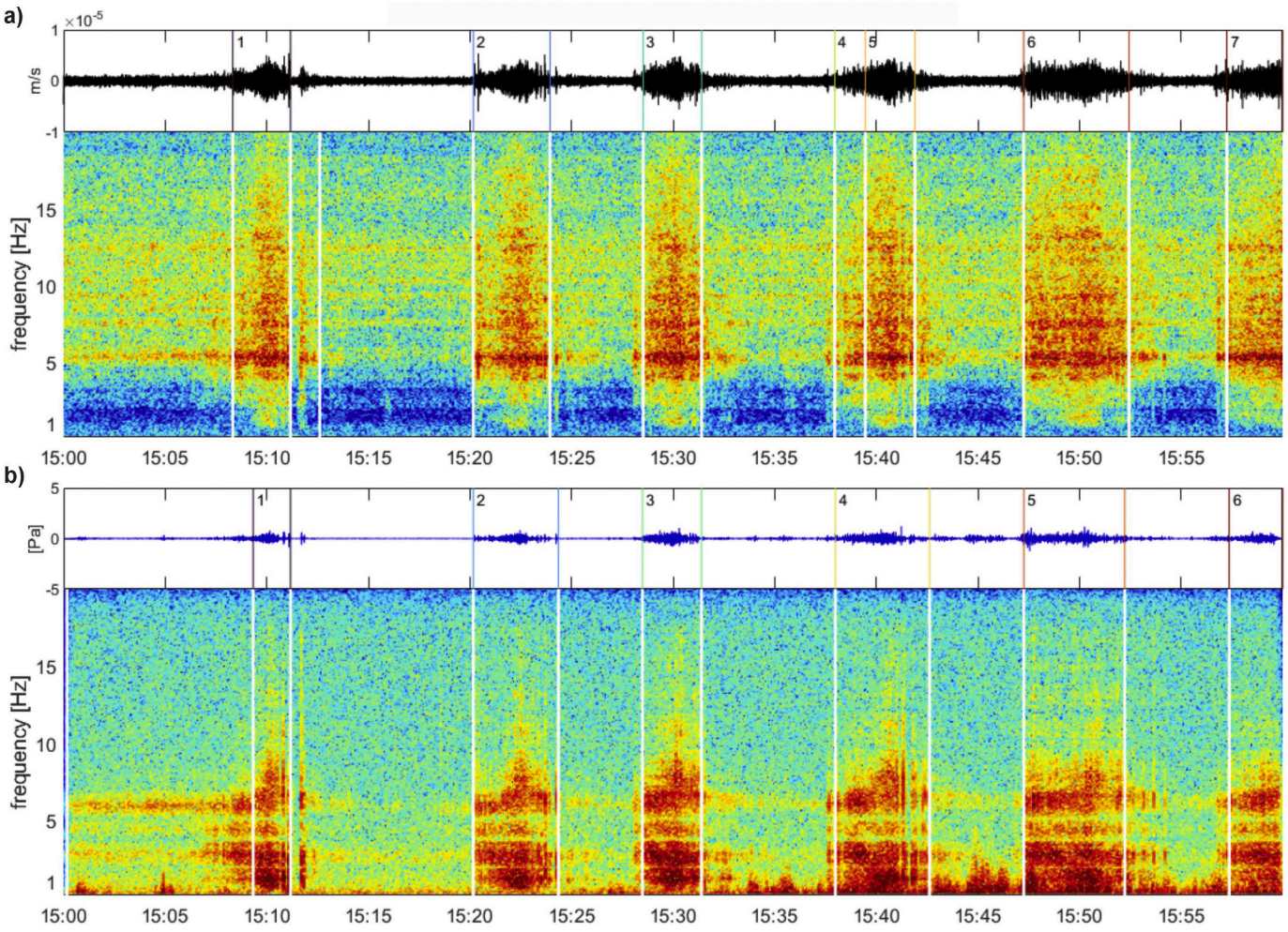

Fig. 2. Example of detected tremors. a) Upper panel shows seismic time series with colored lines indicating start and end of each detected tremor (from the change point analysis) and associated number of tremor occurrence within this hour-long file. The lower panel shows the spectrogram of the time series with the white lines showing every detected change point of the spectrogram. b) Same as in a) except time series and spectrogram are from infrasound data.

repeat our rationale from above using a change point approach on the spectrum and energy calculation between change points to detect acoustic tremors. Accordingly, tremor start and end points in time will differ between seismic and infrasound data because they are derived independently. Additionally, we calculate the cross-correlation between seismic and acoustic data for each detected banded seismic tremor.

3.3. Thermal satellite data

Given the absence of a real-time permanent monitoring network, we rely on thermal data derived from various satellite sensors with IR detection capability to temporally and spatially constrain the eruptive activity at Oldoinyo Lengai. We use products from four different instruments: 1) the Moderate Resolution Imaging Spectroradiometer (MODIS), which guarantees 4 overpasses each day at a resolution of 1 km per pixel, mounted on board Terra and Aqua platforms, 2) the Visible Infrared Imaging Radiometer Suite (VIIRS) mounted on Suomi-NPP and JPSS-1 platforms, with a spatial resolution of 375 m per pixel and 4 images per day, 3) the MultiSpectral Instrument (MSI) on board SENTINEL 2 (S2), acquiring one image every 5 days at a resolution of 20 m per pixel and 4) the Operational Land Imager (OLI) on Landsat 8 (L8) platform, acquiring one image every 8–16 days at a resolution of 30 m per pixel (Coppola et al., 2016; Massimetti et al., 2020; Campus et al., 2022). The granules derived from MODIS and VIIRS instruments are analyzed in the Middle and Thermal Infrared regions (MIR-TIR, wavelength between ~3–5 μm, and 5–12 μm, respectively) of the EM spectrum, while MSI- and OLI-retrieved data are analyzed in the Shortwave Infrared region (SWIR, wavelength ~ 1–3 μm). Data are processed using the MIROVA and HotSpot Thermal Index detection algorithms (Coppola et al., 2016, 2022; Massimetti et al., 2020).

The MIROVA algorithm provides estimates of Volcanic Radiative Power (VRP, in Watt): a measurement of the radiant power released by high-temperature emissions features related to volcanic activity (Wright et al., 2002; Coppola et al., 2016). VRP quantification results from the application of the MIR method by Wooster et al. (2003). VRP values obtained from MODIS and VIIRS images are processed and filtered to avoid errors due to the detection of fake anomalies, unfavorable view geometries and bad weather conditions, as follows: the dataset is composed only of nighttime cloud-free images acquired by satellite at a zenith $<50^{\circ}$, and whose anomalies occur in a 2 km radius from the coordinates of the summit of Oldoinyo Lengai, considering the activity strictly localized inside the summit crater area (see Coppola et al., 2016; Campus et al., 2022 for more details in filtering MODIS and VIIRS dataset). The Thermal Index (TI), from MSI SENTINEL-2 and OLI LANDSAT-8 images, is an empirical and nondimensional parameter considered as a proxy for the pixel-integrated temperature (Massimetti et al., 2020) and has been successfully used to study volcanogenic thermal emission in SWIR bands (Laiolo et al., 2019; Shevchenko et al., 2021). It is calculated as the sum of Top-Of-Atmosphere reflectance values in the SWIR bands only for the hot recognized pixels.

4. Results

The analysis of the year-long seismic data reveals a number of important findings. Generally, seismic tremor is ubiquitous but differs strongly in amplitude, dominant frequency, harmonics and style as well as seismo-acoustic coupling and correlation with thermal anomalies detected by satellite (Fig. 3).

4.1. Seismic amplitude variations

Based on RSAM (Fig. 3a), we detect strong seismic tremor in the beginning of our recording interval in March 2019 which corresponds to long-duration tremors partially consisting of many individual events with high amplitudes and frequency (see Fig. 4a), which slightly subsides and increases again towards end of May. Given the seismic instruments' natural of frequency of 4.5 Hz, all spectrograms in this work clearly show a loss in energy below 4.5 Hz (which is not related to the volcanic signal). Immediately following is an episode of highest RSAM values we detect in ~June through July, which starts with the onset of a continuous seismic tremor on 28th of May (Fig. 4b) leading to a period of intense banded or recurring tremor (Fig. 4c). Here, RSAM values also show the largest scatter, indicating that the tremor signal changes drastically. Average RSAM values are lower from September 2019 onwards with a few episodes of stronger tremor, particularly in December (Fig. 3a). Individual data examples reveal day-long duration tremors with variable amplitudes, sometimes with frequency gliding (Fig. 4d,e).

4.2. Dominant seismic frequencies

Most dominant frequencies lie between 5 and 10 Hz (Fig. 3b). More precisely, in nearly one fourth of individual hours files, the dominant frequency is ~9 Hz. Complementary to the change of seismic tremor style and strength noted by abrupt increase of RSAM in late May, the dominant frequency drops from ~10 Hz to ~5 Hz. After intense seismic tremor subsides in July, the dominant frequency returns to 10 Hz. In August, a second dominant frequency appears at ~7 Hz. After mid-November, dominant frequencies are much more scattered.

4.3. Seismo-acoustic harmonic tremor

Harmonic tremor is a distinct feature of the seismo tremor signal at Oldoinyo Lengai while infrasonic harmonic tremor occurs less frequently (Fig. 3c,d). We detect 9535 min of seismic harmonic tremor, so on average more than one minute of harmonic tremor for every hour of data (if we lower our HSI criteria, we detect >8 min of tremor per hour). The number of detected minutes of seismic harmonic tremor per day varies significantly, often with many detections of harmonic tremor in a few days and longer time periods with few detections. Infrasonic harmonic tremor shows a similar behavior but occurs less frequently overall, with 2485 min of detected harmonic tremor (Fig. 3d). On average, the seismic fundamental frequency is between 1 and 3 Hz, while the first harmonic is between 3 and 5-5.5 Hz. The second and third harmonics each have two significant frequencies between 5 and 6.5 Hz and 7–8 Hz and between 7.5 and 9 Hz and 9.5–10.5 Hz. The infrasonic dominant frequency lies between 0.3 and 0.7 Hz, with the overtones appearing at ~1 Hz, ~1.6 Hz and 2.3 Hz. The occurrence of seismic harmonic tremor seems independent of the strength of tremor as indicated by RSAM and dominant frequencies (Fig. 3a-c) while the occurrence of infrasonic harmonic tremor seems to roughly correlate with higher RSAM values.

Seismic harmonic tremor usually occurs with similar characteristics over longer time periods and often jumps between episodes i.e. mid to end March or end November to beginning of December (see Fig. 5 for a zoom in of Fig. 3c for a several examples). For example, long-lasting seismic harmonic tremor episodes (several days) occur in mid-March, in the beginning of May, and from end of May through June. Interestingly, harmonics are detected more often during times when RSAM is low (see Fig. 3), particularly mid-June where clearly two different sets of fundamental frequencies and harmonics are detected. Visual inspection of week-long spectrograms reveal that similar harmonics are present before, during and after the short tremor ‘pause’ but are much weaker when the dominant 5 Hz frequency is present. In August through September, the mean detected number of minutes of harmonic tremor per day is higher than in the preceding and following months. From the end of November to mid-December, the number of detected minutes of seismic harmonic tremors per day correlates mostly to high RSAM values, albeit with a shift in time. Again, harmonics are present even if RSAM is high but are much weaker (Fig. 3a,c). As in June, frequencies higher than 10 Hz are much less pronounced. The fundamental frequency and its harmonics glide often and over long time periods. We observe gliding over the course of a few hours for example in March,

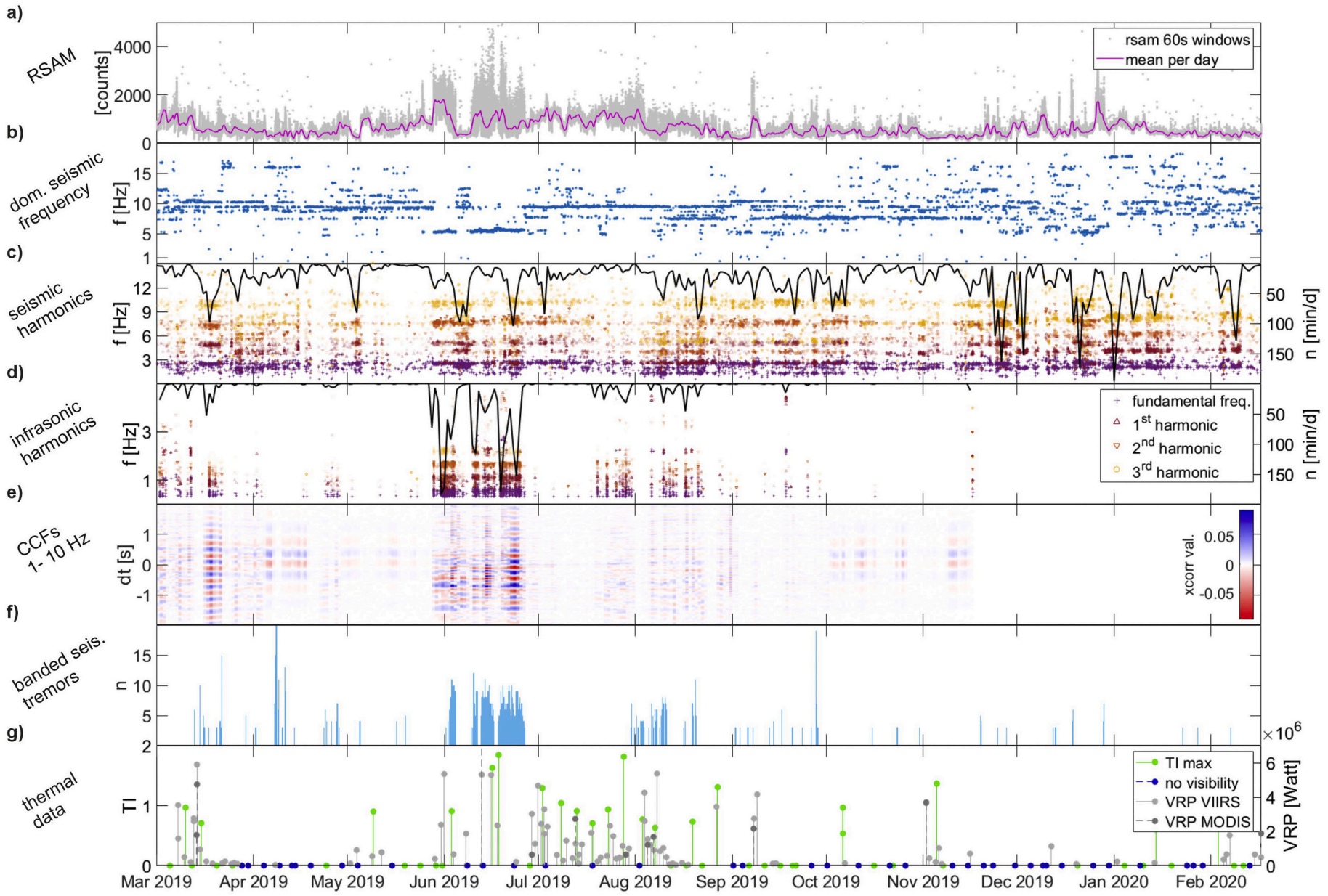

Fig. 3. Year-long overview of time series analysis. a) RSAM for 60 s windows. b) dominant frequency for hour-long time windows. c) seismic harmonic frequencies for minute-long windows: we show the fundamental frequency (purple crosses) and three harmonics (1st harmonic are crimson upward facing triangles, 2nd harmonic are orange downward facing triangle and 3rd harmonics are shown by yellow circles). The strength of the color of the harmonics is based on the HSI value. The black lines indicate the number of minutes of harmonic tremor per day. d) Infrasonic harmonic frequencies, same as c. e) Seismo-acoustic cross-correlation functions per day from stacked hour-long files for 1–10 Hz. f) Histogram of banded seismic tremor occurrences per day. g) TI and VRP from IR satellite data; "no visibility" indicates dates where a direct view of the crater area of S2 and L8 images is obstructed by clouds. (For interpretation of the references to color in this figure legend, the reader is referred to the web version of this article.)

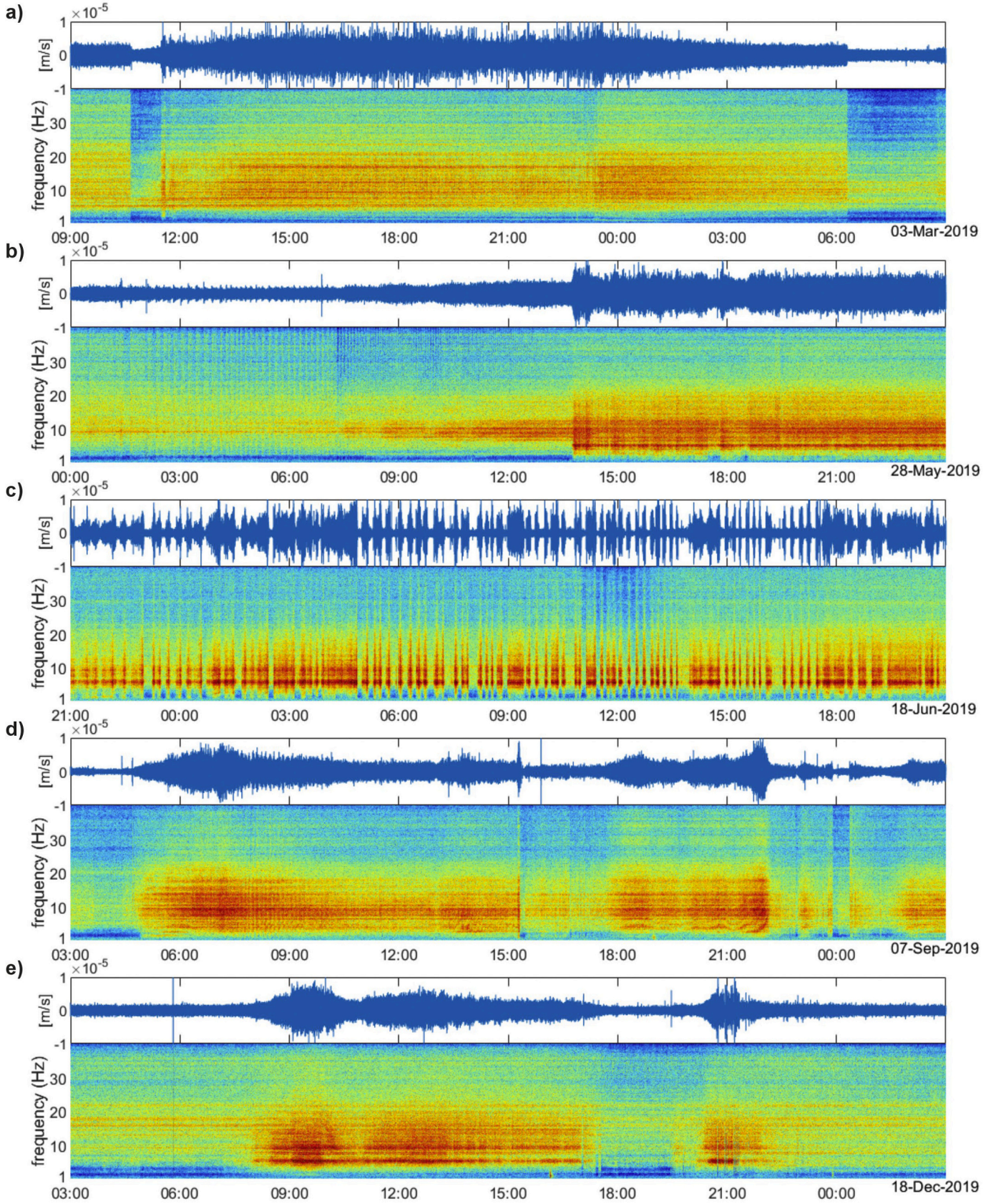

Fig. 4. Examples of seismic tremor in 2019, each subplot shows 24 h of seismic tremor and its corresponding spectrogram, calculated in 10s intervals and filtered between 0.1 and 40 Hz. a) 3rd March, b) 28th May, c) 18th June, d) 7th September, e) 18th December.

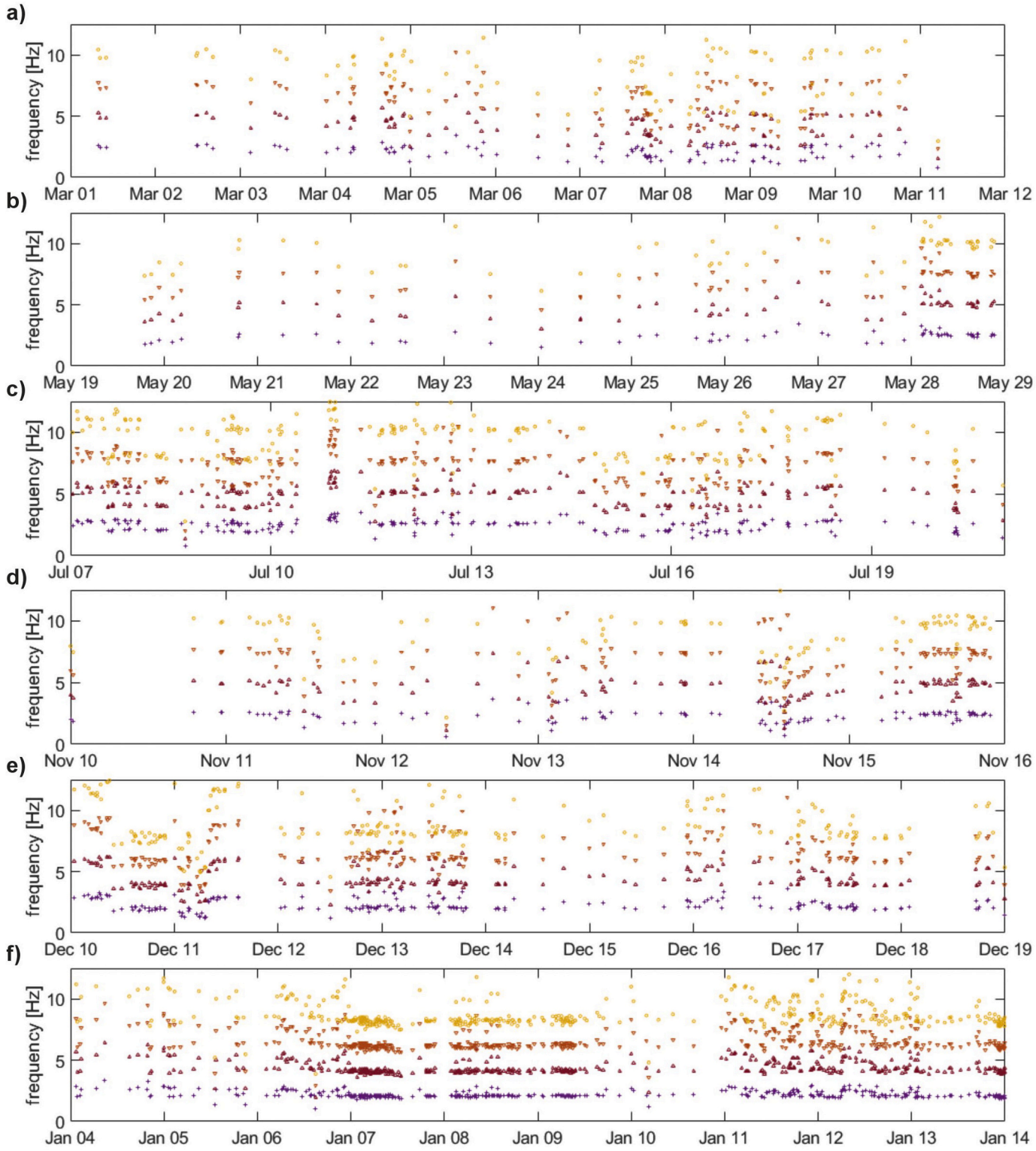

Fig. 5. Examples of seismic tremor with gliding harmonics with same color/symbols as in Fig. 3c. a) March 1st – 12th,b) May 19th – 29th, c) July 7th – 21st, d) November 10th – 16th, e) December 10th – 19th, f) January 4th – 14th.

July, November and December but also gliding trends over days in i.e. May and December (Fig. 5).

4.4. *Seismo-acoustic cross-correlations and coherency*

The daily seismo-acoustic cross-correlation functions (CCF) show different correlation values throughout the year (Fig. 3e). We consider high values to reflect seismo-acoustic tremor. CCF values in April and October – November with noticeable lower frequency are due to wind as confirmed by manually checking the time series. Beginning of March and end of July to end of September show weaker but noticeable correlation values. CCF values are particularly high for a tremor episode in mid-March, for the continuous tremor onset in May (Fig. 4b) and banded tremor in June (Fig. 3e) which corresponds to high RSAM values and the

pronounced drop in frequency (Fig. 3a,b). These tremor episodes also show strong harmonic tremor on the seismogram (Fig. 3c). To study differences in their CCFs in more detail, we consider one-hour segments within these periods. Fig. 6 shows several examples for time series of seismic and infrasound traces, their CCF and spectra. Smaller CCF values in early March and mid-July correspond to infrasound and seismic data with broad-band, continuous tremor with medium high amplitudes (Fig. 6a,d). High CCFs values in mid-March and June are caused by banded tremor on both seismic and infrasound (with an added strong continuous tremor in March; Fig. 6 c,d). Time series and spectra corresponding to high CCFs values end of May are continuous spasmodic tremors on both seismic and infrasound data (Fig. 6e). CCF episodes with lower frequencies such as in April and October – November are caused by strong wind as visible in Fig. 6f. The appearance of wind is characterized by extremely high amplitudes and energy distributed across the entire spectrum (Fig. 6f lowest panel).

To show the details of seismic and acoustic data more clearly, we show 30 s of the traces shown in Figure 7. We find that there some commonalities between the waveforms: examples a), c), e) and b) and d) shows distinct different features. While the first group (examples a), c), e)) is characterized by high frequency and sudden amplitude changes, the latter group consists of lower frequency wave packages which are particularly pronounced on the infrasound data.

We further explore the coupling between seismic and infrasound data by calculating the coherence between the two. Using the approach by Matoza and Fee (2014), we tested the coherency in 20 s windows. We check all hour-long files and show those with the strongest CCF values for comparison (Fig. 8, see Fig. S2 for the examples shown in Fig. 7). Generally, we find that coherency between seismic and infrasound data is only given in a small frequency range (around ~5 Hz; Fig. 8a). For the strongly (banded) tremors, seismic and infrasound data are more coherent but do not display a dominant phase shift expected for ground-coupled airwaves (Fig. 8b, c).

4.5. Seismo-acoustic banded tremors

We apply the detector for banded seismic tremor episodes for different filter bands (i.e. 0.1–20 Hz, 0.5–5 Hz, 1–10 Hz, 5–20 Hz) and find that they largely detect the same signals, but differ in smaller details such as how many tremors are detected and how well they correlate between seismic and infrasound data. We thus show results for 1–10 Hz as this provides the best overview (Fig. 3f). There are single days in which we detect many banded tremors, such as on April 7th – 8th (Fig. 2) and longer episodes of banded tremor detections in June and August. The episode in June follows the onset of the continuous, strong harmonic tremor whose dominant frequency clearly drops to 5 Hz. A small pause of banded tremor detections early-June corresponds to a return to 10 Hz for the dominant frequency.

Taking a closer look at a detailed analysis (Fig. 9), we detect 2675 seismic and 1128 banded infrasound tremors assuming that the tremor does not exceed 10 min, at least three tremors occurred within one hour. We apply an additional criterion for infrasound tremors that their number per hour shall not exceed the number of seismic tremors because too many detections are indicative of wind as confirmed by manual checks. Most tremors have a duration of up to four minutes (Fig. 9 a,b). There is a high correlation between seismic and infrasound waveforms in June, and as previously noted, in August. The maximum cross-correlation value between seismic and infrasound data appears at dominant delay times between 0.2 and 0.3 s and 0.6–0.8 s with some cross-correlations indicating no delay (Fig. 9 c,d). We assume the different delay times are caused by the shape of the correlated waveforms themselves, which often appear in wave packages (see Fig. 7) and have multiple similar peaks in their CCFs. Another explanation could be that different processes (i.e. different eruptive centers) were active at the same time. However, there is no relationship between different delay times and dominant frequencies of the tremors which would indicate that both delay times are caused by the same process or that if different eruptive processes were active simultaneously, they appeared at the same frequency. For some days (i.e. 7th/8th of April) and weak cross-correlation values, the delay times are highly scattered. This occurs when seismic data is not correlated with infrasound data, either because there simply is no correlation or wind obscures any signal on the infrasound sensor. The dominant seismic frequency of these tremors is comparable to the overall dominant frequency as indicated by Fig. 3b (5–10 Hz) while infrasound data is usually at 3 Hz and below.

4.6. Thermal satellite data

We observe periods of stronger thermal anomalies in mid-March and from June through August (Fig. 3g). Notably, in these periods we recognize a higher regime of activity which corresponds to anomalies exceeding Volcanic Radiative Power (VRP) values of 1.85 MW (retrieved by Normal Probability analysis, see Fig. S3 in the Supplementary Material), below which we identify a medium-low regime of thermal activity. We detect most of the strong anomalies in June with the highest VRP value of 12.6 MW on June 12th 2019 and the highest Thermal Index (TI) on 18th June at 1.85. However, the period from July to mid-August shows the largest number of thermal anomalies with VRP values reaching up to ~6 MW. To look at how the location of thermal anomalies changes over time, we use SENTINEL-2 and LANDSAT-8 thermal datasets to build thermogram profiles over the crater area of Oldoinyo Lengai (profile width of 300 m, as the dimension of the crater given by Tournigand et al., 2023, submitted to JVGR) in space and time. Every Thermal Index image with at least one hot pixel that is available between March 2019 – February 2020 has been stacked together along North-South or West-East creating one single column for each acquisition day of the image, containing the TI information inside; then every thermal row has been juxtaposed one to the other to get a thermal profile representing the thermal spatial variation in the period of analysis. This approach was already used to study the spatial evolution of thermal features on open vents (Laiolo et al., 2019) as well as lava dome and volcanic explosive activity (Shevchenko et al., 2021; Coppola et al., 2022).

Our analysis suggests that, in the period of investigation, small anomalies occur frequently in the center of the crater floor, with a general enlargement of the hotspots towards the northern and eastern portions of the crater (see Fig. 10). Moreover, the thermal profiles indicate a variation not just in the main anomalies' location, but also in the magnitude of thermal emission (Thermal Index) with brighter colors indicating higher temperatures, for the wider anomalies occupying more portions of the crater floor, and darker reddish colors indicating lower temperatures, for the smaller and subtle ones (Fig. 10b). In other terms, higher temperatures relate to larger anomalies. These analyses clearly indicate times when more than one thermal anomaly is present. During the first part of our study (March – May 2019), small-sized anomalies are located in the center of the crater floor (Fig. 10a). In June 2019, we detect the strongest thermal signals as described above which is confirmed by the presence of SWIR anomalies with the largest dimensions in the investigated period. This consists of two different locations of hotspots, the main and larger in the middle of the crater and a subtle but visible one on the western edge of the crater, next to the crater wall (Fig. 10a). In July and August, weaker anomalies again first appear in the center of the crater and then migrate North-East. Fewer anomalies are visible in the second half of our study, but mostly consist of single, larger detections. Detections are noticeably diminished in April and May and November – December, possibly because of a heavier cloud coverage due to the rainy season.

5. Discussion

Our observations of one year of data show the richness and wide variety of seismo-acoustic tremor and thermal signals from Oldoinyo

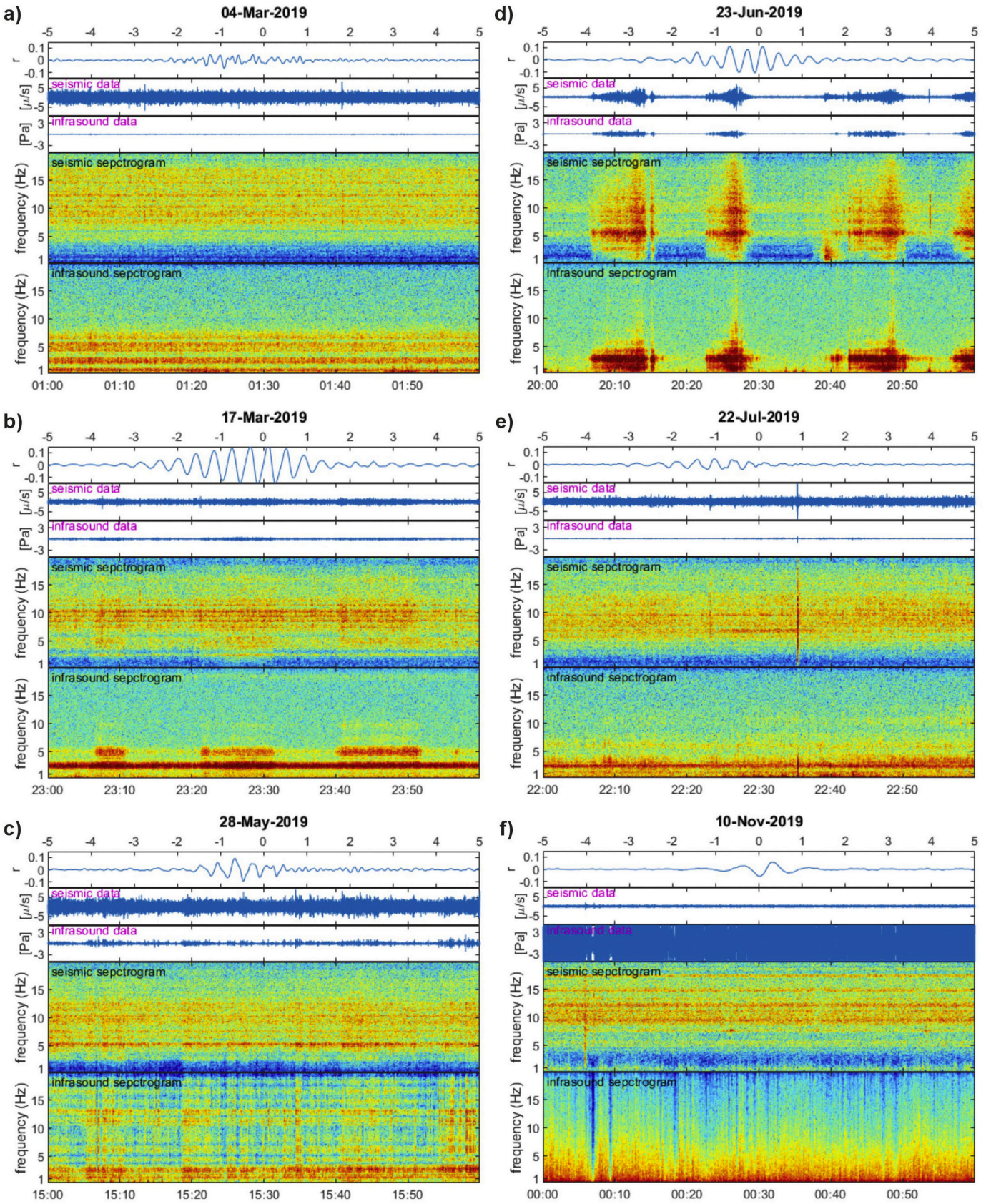

Fig. 6. Selected hour files of seismic and infrasound data. All subfigures show 1) seismo-acoustic CCF for 1–10 Hz where [r] indicates the correlation value, 2) seismic trace, 3) infrasound trace, 4) seismic spectrogram, 5) infrasound spectrogram. a) 4th of March 2019, b) 17th of March 2019, c) 28 of May 2019, d) 23rd of June 2019, e) 22nd of July 2019 and f) 10th of November 2019.

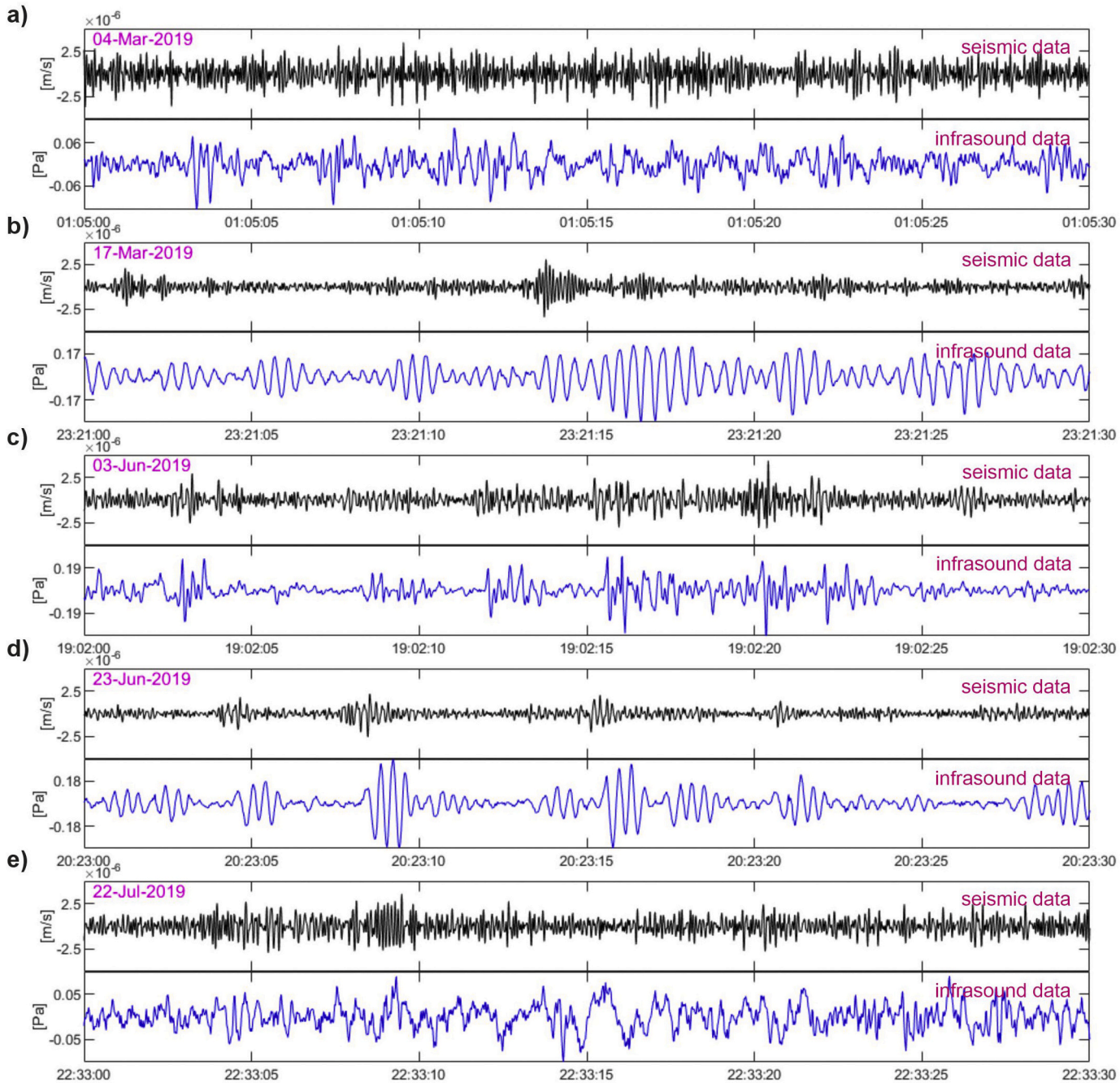

Fig. 7. 30 s of seismo-acoustic tremor from hour files 6a-e. a) March 4th 01:05, b) March 17th 23:21, c) May 28th 15:19, d) June 23rd 20:23, e) July 22nd 22:33.

Lengai volcano which we have illustrated by looking at the data in different time scales and methods. Our investigation offers the opportunity to study the geophysical responses of seismic, acoustic and thermal data to volcano-related activity for this unique volcano. The analyses of our time series often show concurrent changes of their properties, suggesting a possible common volcanic process. To facilitate a better overview of which observed metric changes, Fig. 11 summarizes all data we show in Fig. 3 in a simplified manner, indicating presence or absence and magnitude of each parameter (white to dark shades) over time. We also highlight points in time where changes over many parameters appear simultaneously. First, we will discuss the most evident features of the individual observations and their relationship to each other. Then, we will derive a time line and model of volcanic processes at Oldoinyo Lengai volcano for periods where we have many observations and discuss what we can infer about the shallow plumbing system and its dynamics. Given the richness of this data set, this study can only provide a summary of likely occurring volcanic processes and more in-depth work should be the scope of future studies.

5.1. Seismo-acoustic tremors

In our observation period, seismo-acoustic tremor at Oldoinyo Lengai is a constant occurrence rather than a single phenomenon. Generally, we can characterize seismic tremor at Oldoinyo Lengai by strongly varying seismic amplitudes and duration, high frequency content, many instances of harmonics and frequency gliding. Given the wide variety of seismic tremor, we opt to use RSAM to systematically study variations in seismic amplitude over the course of the ~one of year of data which allows us to get an overview of seismically active periods even if the detection of single events is difficult. In the past, RSAM has been used to

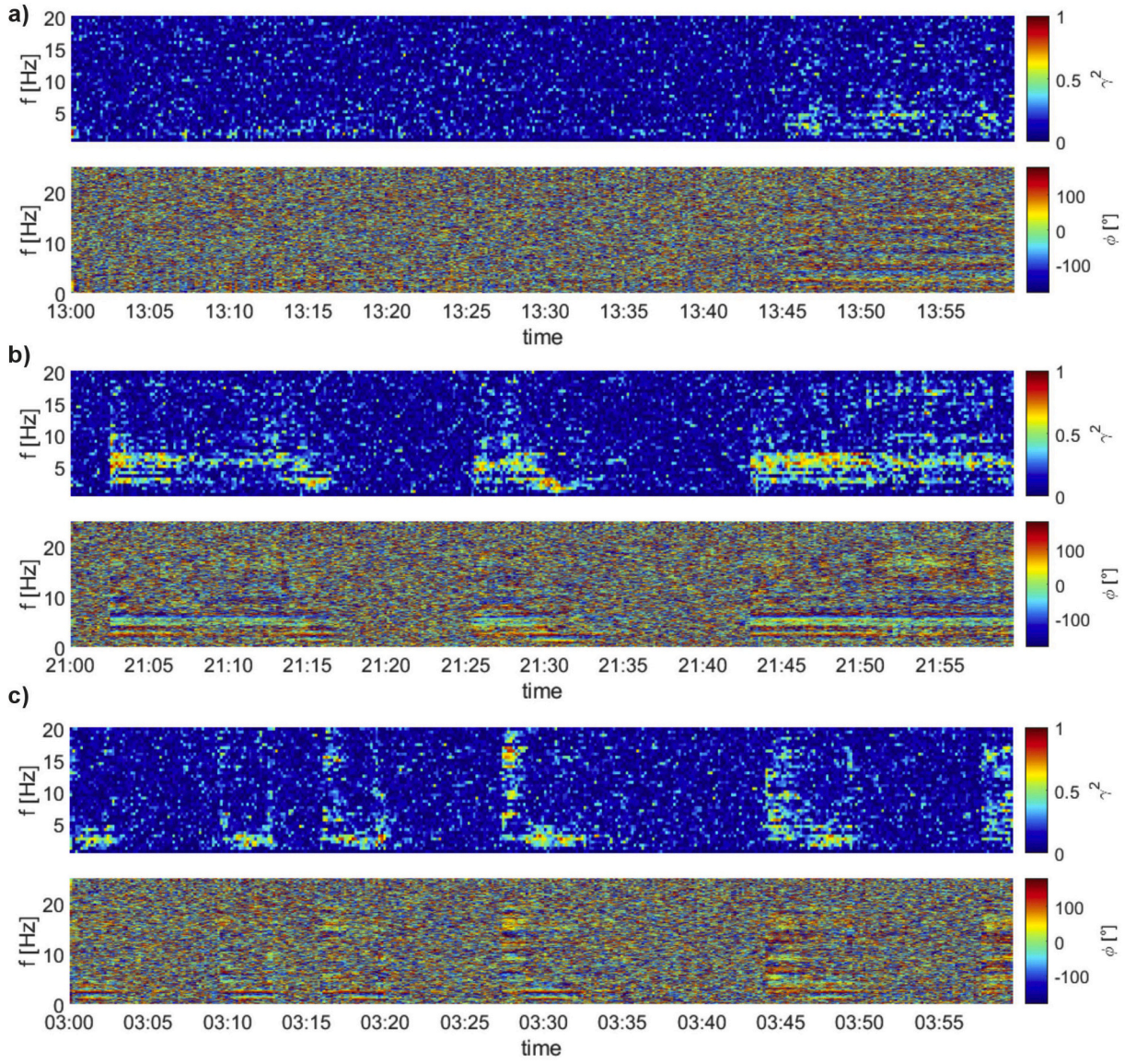

Fig. 8. Example of coherency analysis after Matoza and Fee (2014), upper panel is always coherency analysis and lower panel is phase shift between seismic and infrasound time series. a) 28th May 13:00, b) 3rd June 21:00, c) 11th June 03:00.

detect episodes of i.e. dome growth (Endo and Murray, 1991) or estimates of effusion rates (Aki and Koyanagi (1981); Battaglia et al., 2005) or degassing (Coppola et al., 2009). We interpret that in our data, high RSAM indicates strong tremors caused by volcanic process. However, interpreting RSAM and its changes throughout the year by itself is a difficult task. E.g., we observe week-long episodes of highly fluctuating RSAM in the first half of our data while the average RSAM value is significantly lower in the second half of our observations and is rather characterized by single day-long tremors. Correlating RSAM and thermal data, we often find that high RSAM episodes correspond to thermal anomalies (Fig. 11), which we interpret as volcanic activity at the surface, hinting that RSAM may correlate with eruptions.

Seismic tremor at Oldoinyo Lengai consistently shows much higher frequencies (with tremor energy at least up to 25 Hz, sometimes even with dominant at frequencies larger than 15 Hz) than traditionally expected (i.e. McNutt, 1992). Tremor with high frequencies has been observed during gliding episodes for single occurrences or short time windows, i.e. at Stromboli during the 2007 intrusion (Ripepe et al., 2009) or recurring explosions at Redoubt (Hotovec et al., 2013) but to our knowledge, not as a consistent, ever-present year-long feature. While our ability to capture high-frequency tremor requires recording at short distances due to attenuation of waves travelling inside the Earth's interior (compare e.g. the recordings of Hotovec et al., 2013 across their network), the physical mechanism of what causes these high frequencies is unclear. Hotovec et al. (2013) interpret their observed high frequencies as a series of repeating stick-slip earthquakes near the conduit rather than being caused by i.e. a fluid filled crack. Given the uniqueness of Oldoinyo Lengai's lava signatures (low viscosity and temperature), as well as extremely high CO_2 degassing (e.g. Fischer et al., 2009), we speculate that both of these properties have significant impact on the generation of tremor and thus recorded wavefield. For basaltic volcanoes, Spina et al. (2019) show in experiments that the viscosity of the melt strongly influences the transition among degassing patterns (e.g. from bubbly to slug flow) as well as the recurrence rate of slug bursts at the surface: the lower the viscosity, the smaller the inter-event time. Other studies which focused on explaining frequency gliding have shown that a change in inter-event time will also lead to a change in the observed frequencies (i.e. Neuberg et al., 2000; Hotovec et al., 2013). If we assume that seismic tremor at Oldoinyo Lengai is connected to eruption processes (fluid dynamics and bubble bursting), then the high

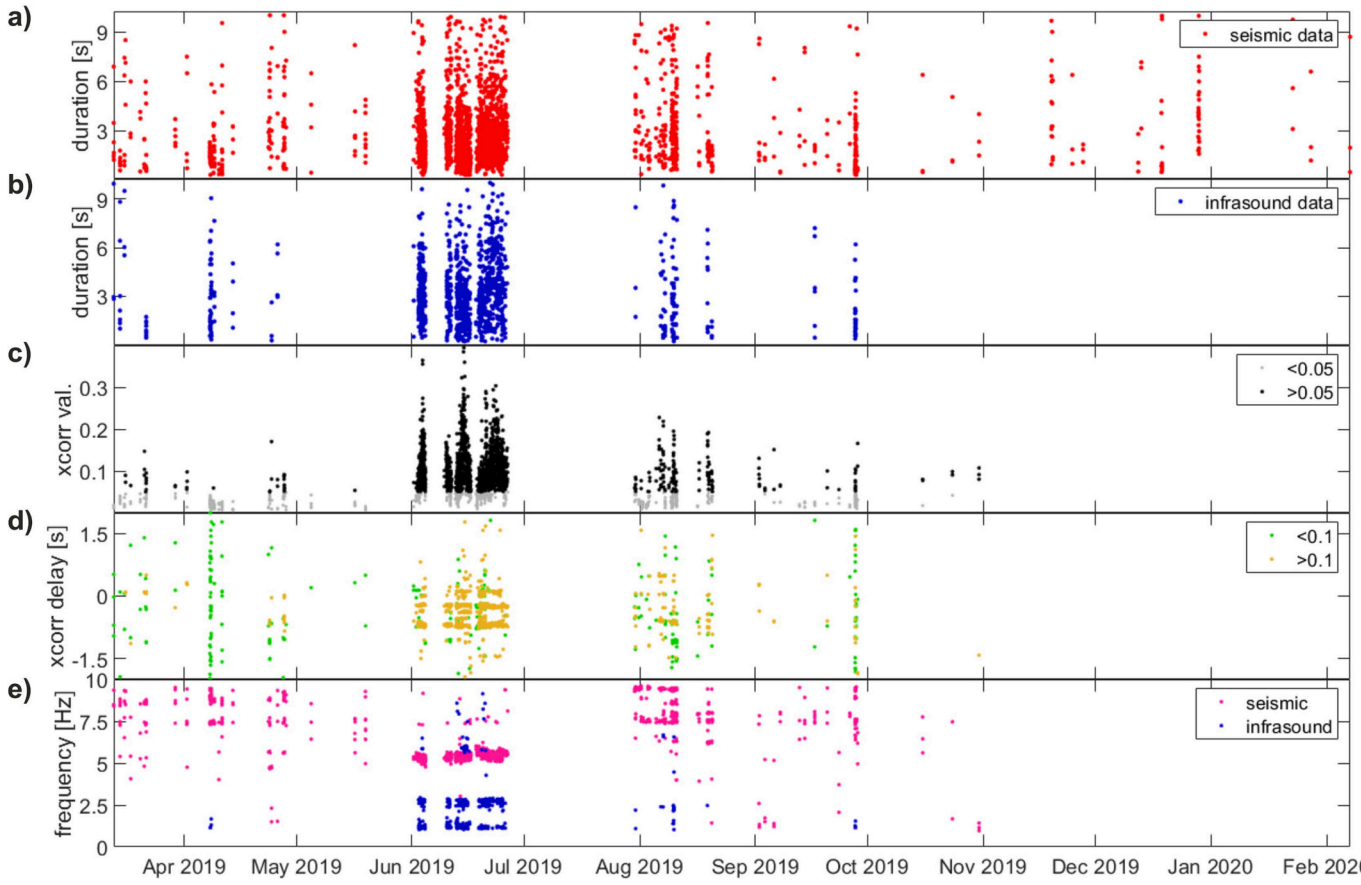

Fig. 9. Overview of detected banded tremors for 1–10 Hz. a) seismic tremors. b) infrasound tremors. c) cross-correlation value. d) delay time corresponding to maximum correlation value. e) dominant frequency of seismic and infrasound tremors.

frequency content may be caused by a very small inter-event time facilitated by the low viscosity of carbonatite melt and high CO_2 content. Analogue experiments and comparative studies between volcanic systems of differing viscosities may be needed to address this issue in the future.

The seismic harmonic tremor we observe (for which we only note the fundamental and three overtones) is also high in frequency content. The underlying causes for seismic harmonic tremor are an active field of research. It has been observed as a precursor before eruptions, i.e. explosions at Redoubt (Hotovec et al., 2013); at Popocatepetl during dome growth (Arámbula-Mendoza et al., 2016) and before explosions (by Roman, 2017) but also as background or syn-eruptive tremor (Neuberg et al., 2000) or during dike intrusions (Ripepe et al., 2009). Models for harmonic tremor sources include resonance in fluid-driven cracks where overtones are produced by standing waves (Chouet, 1988), evenly spaced repeating events (Neuberg et al., 2000); caused by non-linear fluid flow (i.e. chocked flow, Hellweg, 2000) or non-linear responses to fluids flowing through narrow conduits and interacting with the wall (Julian, 1994). In a modeling study, Girona et al. (2019) could show that a steady influx of gas into a gas pocket can cause pressure oscillations which are recorded as harmonic tremor on seismograms while unsteady gas flow may lead to monochromatic or broadband signals depending on the size of the gas pocket. The transition between flow regimes/ gas pocket sizes can also cause gliding. If we compare RSAM, harmonics and thermal data, we infer that harmonics are present during volcanic activity at the surface but also appear when no thermal anomaly is present (Fig. 11). Accordingly, different processes may cause different episodes of harmonic tremor and will be discussed below.

Our observations of acoustic tremor are sparser compared to seismic tremor as our analysis is heavily hindered by wind conditions at the summit of the volcano. We have thus omitted the analysis of dominant frequencies (because those most often simply represent wind), but we frequently observe tremor during non-windy times or super-positioned with wind. Acoustic tremor can be related to all kinds of processes at volcanoes, such as degassing (e.g. Ripepe et al., 2010; Fee et al., 2010), bubble bursting (e.g. Jolly et al., 2016) or explosions (e.g. Johnson, 2003). We will discuss mechanisms of acoustic tremor excitation for specific time periods below. Additionally, the acoustic wavefield is characterized by harmonics (Fig. 3), which has previously been observed at e.g. Halemaʻumaʻu (Kīlauea, Hawaiʻi; Fee et al., 2010) and has been related to the resonance of a gas-filled cavity and used to infer crater geometry. It can further be used to track changes of the level of lava lakes and be used as a predictive tool (Johnson et al., 2018). We detect acoustic harmonic tremor during episodes which are also characterized by high RSAM (Fig. 11), which also often corresponds to detection of satellite anomalies, indicating that our observed signals reflect a common source exciting acoustic and seismic tremor during periods of i.e. open-vent activity such as effusions or surface bubble bursting which are also visible on the thermal data. We rarely observe (harmonic) infrasound during low RSAM episodes (expect for mid-March, see Fig. 11) which suggests that harmonic infrasound is mostly connected to eruptive processes.

Further analysis of seismo-acoustic tremors and their source comes from the correlation between seismic and infrasound data. High seismo-acoustic correlations have often been observed at open-vent volcanoes, such as Stromboli (e.g. Ripepe et al., 1996), Etna (Laiolo et al., 2019), Villarica (e.g. Ripepe et al., 2010; Rosenblatt et al., 2022), Nyiragongo (Barrière et al., 2018) and indicates a common source process which must be close to the surface. Kervyn et al. (2008) inferred a connected shallow plumbing system within the plateau which enclosed the summit

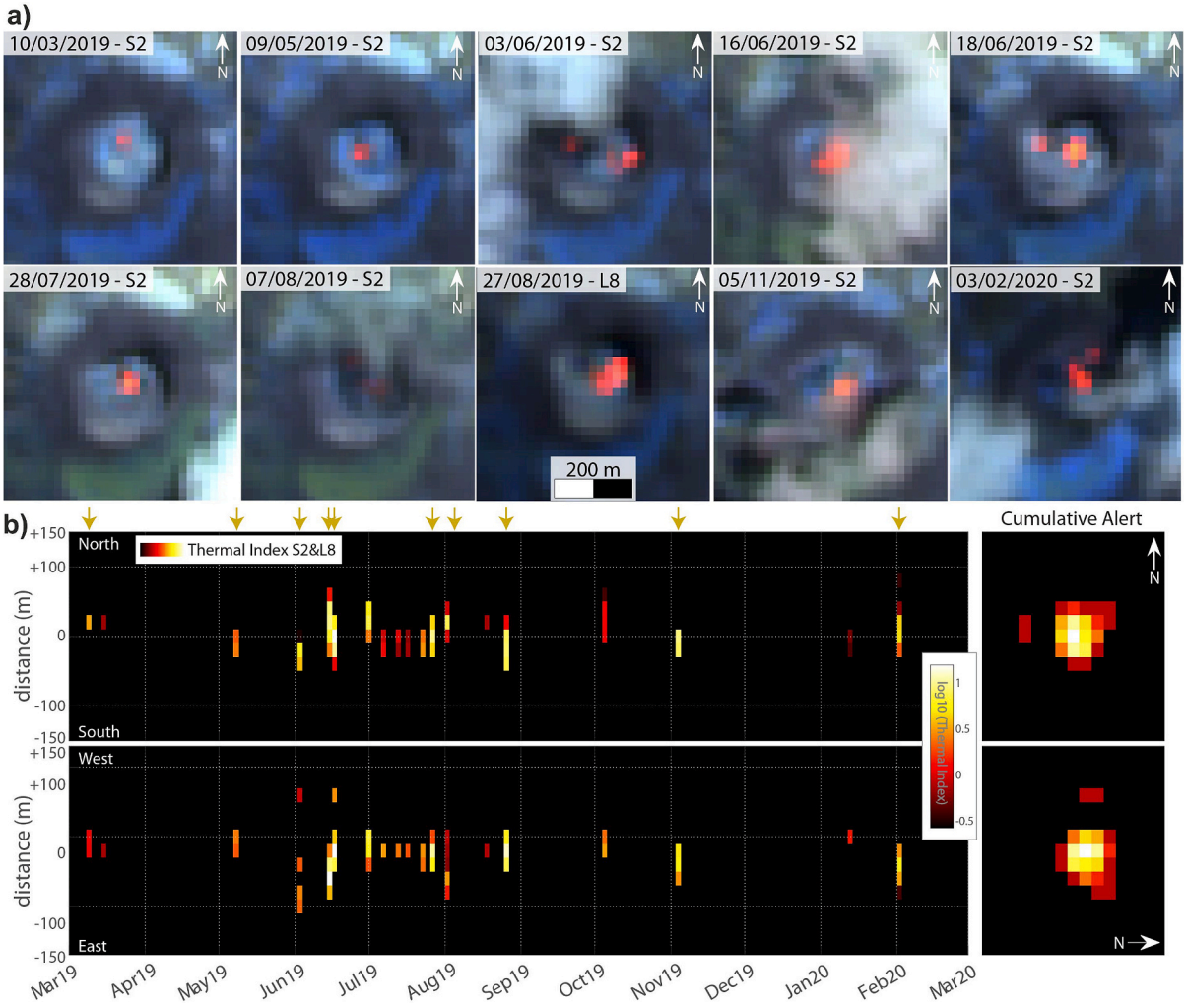

Fig. 10. Thermal data from MSI-Sentinel 2 and OLI-Landsat 8. a) images from dates as indicated by the legends, b) stacked thermal profiles (aligned N-S and W-E) along the summit area of the volcano (dimension of 300 m). Colors from red to bright yellow represent the increasing intensity of heat emission represented by Thermal Index values. Small yellow arrows on the top indicate the point in time of images shown in a). (For interpretation of the references to color in this figure legend, the reader is referred to the web version of this article.)

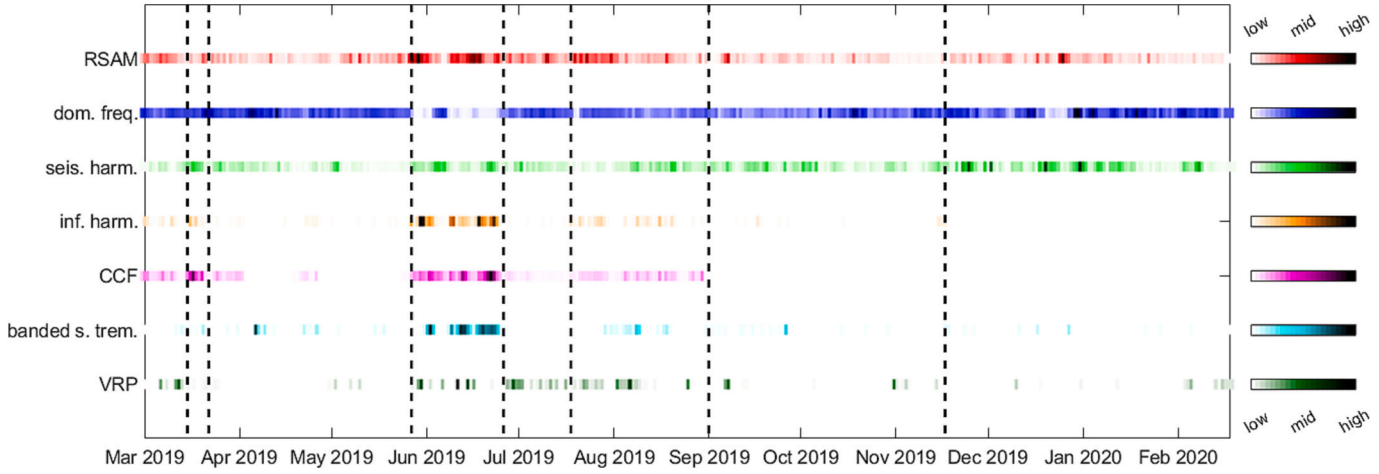

Fig. 11. Simplified summary of observed parameters based on results in Fig. 3. All data have been normalized to values between 0 and 1, where the color scale for each parameter always varies from white, indicating low or small values, to black, indicating high or large values. In the center of each color scale is a solid color for differentiation of parameters. Vertical dashed lines highlight points in time where several parameters change at the same time.

before the 2007 eruption. They showed a central melt storage cavity supplying melt to hornitos as well as a lava pond and indicated the fast evolution of crater morphology in 2006 which saw the collapse of three hornitos in less than two weeks. Throughout 2019, the crater morphology also changed significantly (Tournigand et al., 2023) and hornitos as well as a lava pond were present (GVP, 2019). We observe high values of seismo-acoustic correlations for episodes with strong and medium-strong tremor as indicated by RSAM, which may or may not be correlated with thermal anomalies (see Fig. 11, compare periods in March vs. end of May/June which we describe in detail in the next section). Accordingly, seismo-acoustic tremors may be caused by different sources: some with and some without heat signatures at the surface, most likely eruptions with lava output or degassing processes close to the surface.

Finally, the seismo-acoustic wavefield is characterized by many instances of frequency gliding. This can be observed in the harmonics (Fig. 5), but also for individual frequency bands, mostly for seismic data but sometimes also for the acoustic data (see Fig. 11). Gliding is not restricted to particular frequency bands, time intervals or occurrence length. Generally, source models for gliding are based on time-dependent changes in the medium or the source (e.g. Aki and Koyanagi, 1981; Hotovec et al., 2013). Many studies have observed frequency gliding in various contexts, such as during eruptions (e.g. Neuberg et al., 2000), preceding explosions (Hotovec et al., 2013), intrusions (e.g. Ripepe et al., 2009) or reflect a rising magma column (infrasound gliding: Sciotto et al., 2022). However, no study that we are aware of reports the number of different types of gliding events, particularly long-lasting gliding events. From visual inspections of daily to weekly spectrograms, we estimate at least ~85 individual gliding events ranging from hours to days with many more detected if we consider the harmonic analyses. While a detailed investigation is beyond the scope of this study, there are some indicators for different processes: In times where changes in the acoustic data are present, this may point to a change in the resonator (see Fig. 12a, i.e. Fee et al., 2010), a change in the lava lake level (Johnson et al., 2018) or a change of the speed of lava eruption, i.e. a change in jetting (Gestrich et al., 2022). Unfortunately, wind prohibits this conclusion in most cases (e.g. Fig. 12b,d). In cases where individual events are visible and the same gliding mechanisms repeats (Fig. 12c), this may be caused by a change in inter-event time between repeating events as suggested by Neuberg et al. (2000) possibly due to a change in gas content (Benoit and Mcnutt, 1997). Fig. 12e and Fig. 4d looks similar to data from a dike intrusion at Stromboli (Ripepe et al., 2009). The (monotonic) gliding in Fig. 12d and f are more puzzling. As a mechanism for long-term gliding, which far exceeds timescales of rising magma, Unglert and Jellinek (2015) suggest bubble cloud oscillations and evolving magma dynamics related to the geometry of the plumbing system. In summary, the many instances of gliding may reflect a multitude of processes, but it is likely that the geometry of plumbing system changes throughout our observation period as outlined in section 5.3.

5.2. Thermal eruptive signals

To first order, we use thermal satellite-based data to identify periods of eruptions or lava flows. This has three caveats: the standard impairment of satellite measurements which requires clear line-of-sight, Oldoinyo Lengai's relatively cold lava temperatures of ~550 °C (e.g. Fischer et al., 2009) which means quick cooling and satellites may miss the thermal anomaly by a few hours and a coarse resolution in time overall. However, using both TI and VRP parameters by SWIR high-resolution (S2 and L8) and MIR moderate (MODIS and VIIRS) sensors, we can adequately detect, locate and quantify episodes of heat flux release, related to episodes of lava extrusion and/or hot release by fumaroles. Indeed, the phase between 2019 and 2020 we discuss here actually starts in the last months of 2018, and is the highest thermal activity period if we consider the last few years of heat flux emission (VRP), after the previous explosive eruption in 2007–2008 (see S1).

Correlation between seismic amplitude and satellite-derived thermal data observed in several case studies (i.e. Coppola et al., 2009, 2016; Valade et al., 2016; Laiolo et al., 2019) suggests that an increase in seismic tremor (RSAM) and thermal emissions (VRP and/or number of hotspots) generally occurs in relationship to magma ascent to shallower levels and surface magma extrusion episodes. In the investigated period here, thermal satellite analysis clearly shows two main patterns, which are representative of different types of surface volcanic activity of Oldoinyo Lengai volcano (Fig. 3g and Fig. 10). The first is expressed by wider anomalies with higher VRP and TI values (max. VRP of 12 MW on 12th June 2019 and max. TI of 1.85 on 18th June 2019) related to episodes of production of lava flows in the central part of the crater occurring in June, end of August, and September 2019. Moreover, in this period, an additional feature is represented by the presence of a hotspot in the western part of the crater floor is evident in June 2019, indicating the production and activity of a new hornito, or small lava pools, as also described by field visual inspection and phots (GVP, 2019). The second type of thermal activity is related to a stable presence of small thermal anomalies, particularly during July–August 2019, but also observable in other period such as March 2019 and mid-September 2019, in the central part of the crater (around 225 px in the N-S profile Fig. 10) with reddish dark colored tones (low TI), while VRP fluxes reach maximum ca 4 MW, indicating a localized, low-temperature thermal hotspot. All these episodes are associated to periods of increased RSAM, and some are associated with more intense seismo-acoustic correlations, and banded tremor (Fig. 11). We will use these to distinguish different volcanic processes below.

5.3. Volcanic processes at Oldoinyo Lengai

Following our discussion of seismic-acoustic tremor and thermal signals, we identify different volcanic processes of Oldoinyo Lengai throughout the ~one year of data based on point in time where many of our observed paramters change simultaneously, invoking a common volcanic process: 1) intrusive activity and/or possibly construction of large hornito, which is characterized by high seismic amplitudes and many detections of harmonic tremor but shows no evidence of thermal anomalies, 2) degassing, with strong correlation between seismic and acoustic data and harmonics and the absence of/or presence of minor thermal anomalies, 3) weak effusive or stationary activity of a lava pond with many detections of thermal anomalies, few harmonics and weaker correlations between seismic and infrasound data, and 4) strong extrusive activity, which is characterized by day-long high seismic amplitudes with harmonic tremor, good correlation to infrasound data, possibly banded tremor and existence of higher thermal anomalies. In the following, we discuss the changes of volcanic activity over the course of the year (see Fig. 13a for a timeline and 13b-g associated processes). Additionally, we show the associated seismic and acoustic spectra for a week of each inferred period in Fig. S4. We note that there are periods in time that we do not discuss because our observed parameters are not distinctive enough to allow an interpretation.

5.3.1. Beginning of March: Extrusive activity

The beginning of our study period in March is marked by the appearance of medium to high thermal anomalies, with VIIRS-retrieved VRP values reaching a peak of 5.89 MW on 12 March 2019, high average RSAM values and good correlation between seismic and infrasound data. Both also show weak harmonics, as indicated by Figs. 3 and 11 and a closer look at Fig. 6a shows a dominant frequency with three overtones for the infrasound data. Waveform data show impulsive signals that may be caused by minor explosions or bubble bursting (e.g. Fee and Matoza, 2013; Jolly et al., 2016) which may be the source of seismo-acoustic correlated wavefield. Fig. 12a also indicates gliding seismo-acoustic harmonics which may represent a change of the resonator of/within the crater. High-resolution S2 and L8 images indicate the thermal

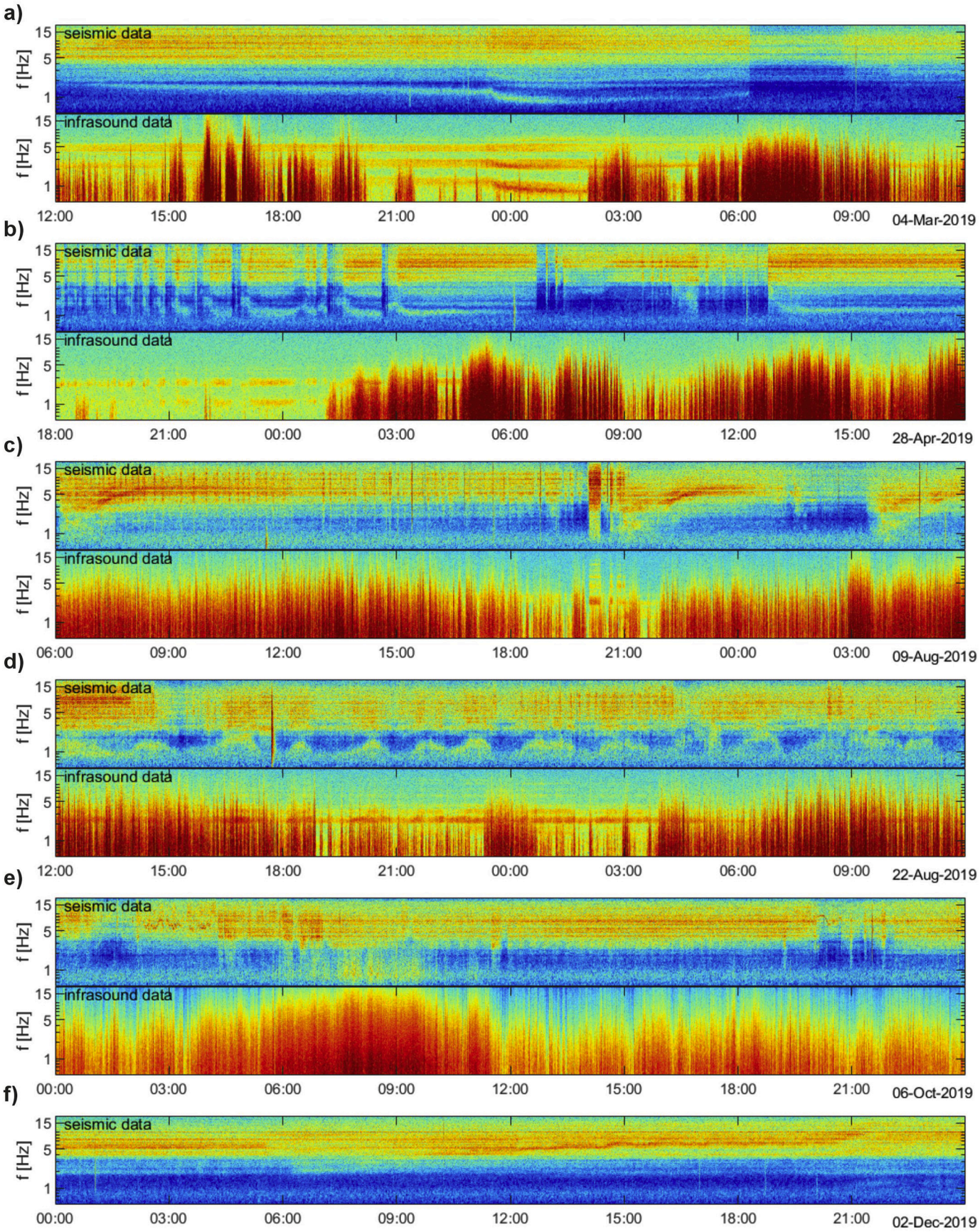

Fig. 12. Examples of frequency gliding from 24 h of data. For each subplot, the top panel is a spectrogram of the seismic trace while the bottom panel corresponds to a spectrogram of the infrasound except for f) where only seismic data is shown. a) Data beginning 3nd March 12:00. b) Data beginning 27th April 18:00. c) Data beginning 8th August 6:00. d) Data beginning 21st August 12:00. e) Data beginning 6th October 00:00. f) Data beginning 2nd December 0:00.

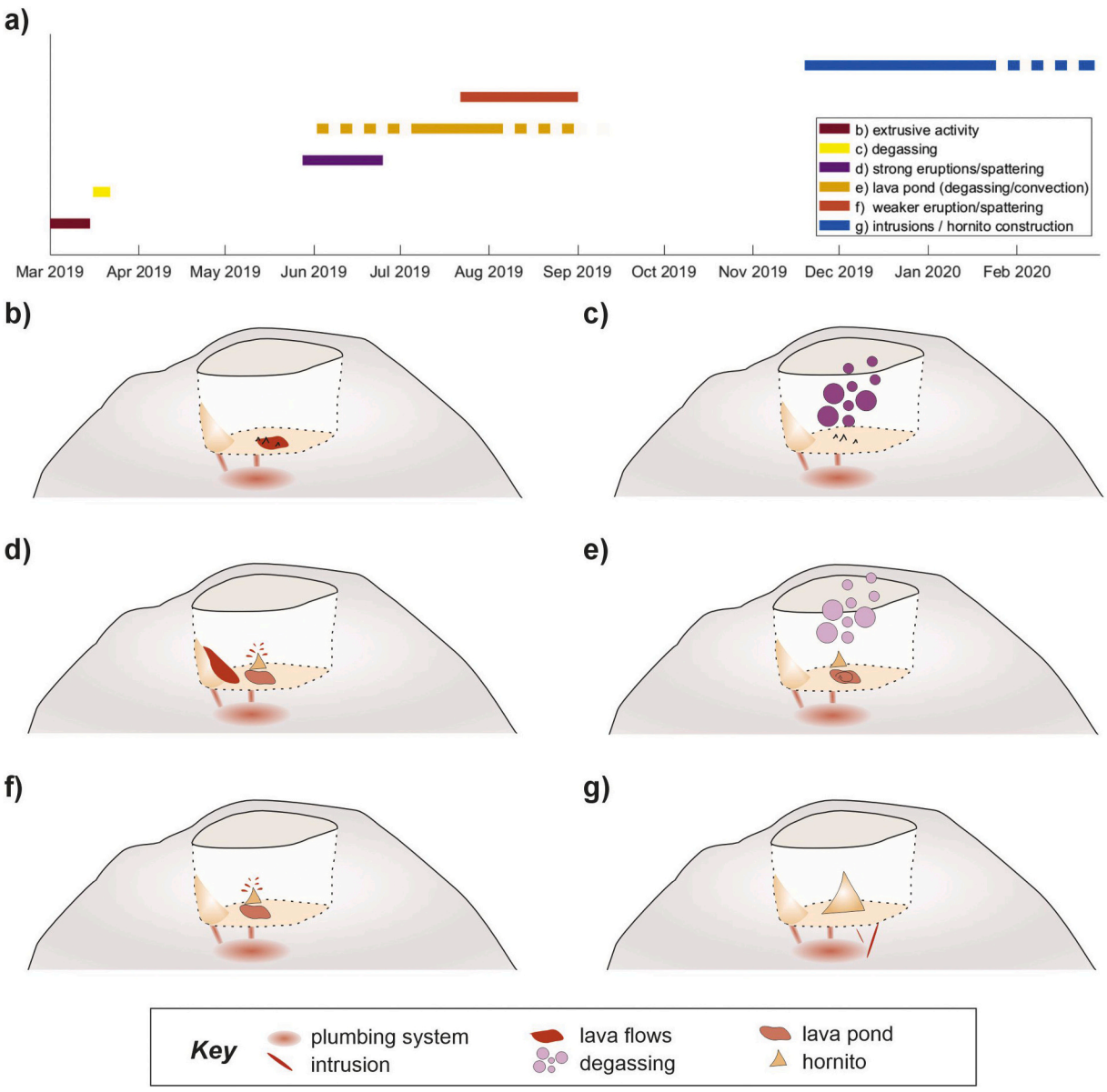

Fig. 13. Inferred Volcanic processes at Oldoinyo Lengai volcano. a) timeline of volcanic activity indicating the approximate date of the specific volcanic activity shown in b) to g). Summit and crater are to approximate scale, structures within the crater are not. b) extrusive activity with lava flows, c) degassing from fumaroles, d) strong eruptions and spattering, e) degassing or convection of stationary lava pond, f) weaker eruptions, g) intrusions and/or constructing of large hornito.

anomaly lies slightly north of the center of the crater. Together, this indicates an eruptive phase with significant perturbation of the atmosphere and likely changes of the eruptive centers within the crater (Fig. 13b; e.g. Coppola et al., 2009; Fee et al., 2010; Eibl et al., 2017).

5.3.2. *Mid-March: Degassing*

This phase is followed by the occurrence of strong seismo-acoustic CCF with lower frequencies (Fig. 6b,7b), strong seismic and infrasonic harmonics and minor/few thermal anomalies (with clear view of the crater) which we interpret as signals of lower temperature that may be caused by fumarole activity rather than lava flows. The infrasound data in Fig. 6b clearly shows the presence of two separate signals, one continuous, dominant ~2.5 Hz tremor and one recurring minutes-long tremor with 5 Hz which is also weakly present in repose times (i.e. times inbetween stronger signals; and weaker over tones). A similar behavior is weakly noticeable for the seismic data. Fig. 7b further shows that waveforms are monochromatic, which also been observed at Villarica (Ripepe et al., 2010) and interpreted to reflect conduit convection dynamics where the monochromatic infrasonic signal likely reflects flow instabilities in the upward rising bubbly column within the conduit or a continuous low-frequency tremor is caused by continuous degassing of a lava lake coupled with the unique resonance features of the crater (Rosenblatt et al., 2022, see Fig. 13c). Considering the results of Girona et al. (2019) we discussed earlier, one could also consider the change in observations from beginning to mid-March in terms of changes in gas flux or subsurface cavity changes. Permanent degassing measurements would help to decipher these processes significantly.

5.3.3. *End of May to end of June: Strong extrusive / spattering Activity*

We interpret our observations from end of May to June, which correspond to the strongest signals we observe in all individual time series (Fig. 11), as a second phase of strong extrusive activity (Fig. 13d). On 28th May, we observe the onset of a continuous tremor with strong seismic and infrasonic amplitudes. The dominant frequency drops distinctly to 5 Hz and we detect many harmonics in seismic and infrasound data which also correlate well (Fig. 3, Fig. 6c). Waveforms,

particularly the infrasonic ones, are extremely impulsive during the onset of the continuous tremor (Fig. 7c). The abrupt decline in frequency coincides with the activity from two different eruptive centers, which is unique to this period, as indicated on satellite images (Fig. 10a): Sentinel images on 3rd and 18th of June indicate two separate sources each. The thermal anomaly to the west is caused by a growing hornito connected to the crater wall while the central anomaly is likely caused by a lava pond (Fig. 10a; GVP, 2019). The continuous tremor evolves into strongly banded tremor from June 2nd onwards. Seismic and infrasound waveforms change their frequency content to lower frequencies and are less impulsive after June 20th (Fig. 7d).

We interpret the sudden onset and the impulsive waveforms early in the sequence as spattering or minor Strombolian eruptions (compare e.g. Sciotto et al., 2022; Fee and Matoza, 2013) which may contribute to building the hornitos (as observed for a later, less intense period in August). The change in tremor may reflect the transition of the opening of the surface of the crater floor for the successive formation of the lava pond (which did not exist in March 2019) while the decline in impulsivity of the waveforms may indicate the eruption is less forceful or changing towards degassing as seen in mid-Mach or that a change in e.g. crater morphology has occurred.

The existence of coupled seismo-acoustic banded tremor hints at a very shallow storage of melt. Cannata et al. (2010) interpreted alternating seismic-acoustic banded tremor at Mt. Etna as caused by recharge-discharge processes in shallow aquifers where heat and fluids are transferred from the main conduit into an off-set shallow aquifer. During phases of recharge, seismic tremor is generated by the influx of fluids which, over time, creates pressure leading to discharge, which then produces an infrasonic signal. As we observe concurrent seismo-acoustic banded tremor, we assume the observed seismic tremor is possibly a superposition of ground shaking (higher frequencies) and ground coupled airwaves from the acoustic eruption signal (lower frequencies) while the infrasonic tremor is a superposition of the eruption signal and possibly resonance from the crater, eruptive bodies and/or shallow fluid-filled cavities (e.g. Matoza et al., 2010; Fee et al., 2010; Rosenblatt et al., 2022) which may have existed during this time and would be in line with previous analysis of crater morphology of a connected plumbing system as outlined above (Kervyn et al., 2008). However, in the absence of an imaging analysis of the crater, we can only speculate to the structure of the crater floor and cavities.

During a phase of relative quiescence in the beginning of June, dominant frequencies abruptly change from 5 Hz to ~10 Hz and we detect more minutes of seismic harmonics tremor with differing fundamental frequencies while the infrasonic harmonic tremor disappears. This may indicate the background seismic tremor caused by subsurface processes is not connected to the bubble bursting or eruptions, as infrasonic harmonic tremor is absent during that period.

5.3.4. July: Stationary lava pond

In July, seismic amplitudes remain high but banded tremor as well as strong seismo-acoustic CCFs disappear while we observe many and increased thermal anomalies. While wind is present and may prevent better recording of the acoustic data and hence stronger coupling between seismic and infrasonic data, acoustic tremor is visible elsewhere during different phases with similar wind levels. Satellite data indicates a unique and stable thermal source which could be likely related to a central active crater feeding in the nearby small short-lived lava flows and hot degassing (Fig. 10a, S2). These analyses correspond well to the local observation of a small active lava pond near the center of the crater (GVP, 2019). In late July, infrasound data appears to be monochromatic and comparable to mid-March (Fig. 6b,e). Accordingly, average high RSAM measurements may reflect the convection of the lava within the pond, degassing, or resonance in the shallowest part of the plumbing system beneath the crater floor (Ripepe et al., 2010; Rosenblatt et al., 2022), similar to a shallow plumbing system which Kervyn et al. (2008) observed prior to the last eruption in 2007 (Fig. 13e). However, given our limited time series of one year, we lack the data to support one hypothesis over the other. To estimate whether the pond is convecting like i.e. magma at Stromboli (Laiolo et al., 2022), we would need estimates of the magma supply and mass eruption rate for which we would need $S0_2$ degassing as well as detailed mapping of lava outputs.

5.3.5. End of July to August: Weaker spattering Activity

CCFs indicate a seismo-acoustically coupled wavefield from late mid-July onwards with some seismic but stronger infrasonic harmonics. Weakly banded tremor reappears on July 24th but is only recognized by our algorithm from July 30th onwards where it is stronger. A significant drop in seismic amplitudes is accompanied by a new dominant frequency at ~7.5 Hz and lower frequency harmonics. We observe many instances of gliding in the strong harmonics whose fundamental frequency is at ~1 Hz. Thermal data indicates a high level of thermal activity throughout this phase, with large thermal anomalies at the end of August (Fig. 10), suggesting that lava is present but seismo-aoustic data indicate a weaker episode than the previous one. We suggest that the phase in July to August represents the change from a stationary lava pond to mild spattering eruptions and lava flows production (Fig. 13f).

5.3.6. Mid November to mid-January: Potential intrusive Activity and large Hornito built-up

From September onwards, seismic amplitudes as indicated by RSAM are low except for some isolated episodes. However, a new phase of activity begins mid-November with many day-long tremor signals with high amplitudes. Unfortunately, the infrasound station stopped working on November 17th which makes it impossible to assess the acoustic nature of these tremors. There is a notable absence of thermal anomalies but the view of the crater was also often obstructed. Assessing the spectrograms and waveforms in more detail as the only permanent observation in this period, the data indicates intrusion style signals are observed in at Stromboli (Ripepe et al., 2009; Fig. 12f). Future data analysis may provide estimates whether these and all other observed signals in this paper occur in the edifice or shallow part of the plumbing system or deeper.

We know from pictures (personal communication from tourists who visited the crater in January and February 2020) that a significant hornito grew over the area of the lava pond (also visible as shadows on a Sentinel 2 image in the visible band in Fig. S5). By January 2021, it reached a height of 55 m from the crater floor (Tournigand et al., 2023, submitted to JVGR). Accordingly, strong harmonics and abrupt changes of their frequencies within this phase may signify this drastic change in crater morphology (Fig. 13g). Though we do not have infrasound data to corroborate this and are lacking information about the crater geometry before and after appearance of this hornito, we suspect a hornito of that size likely changes the resonating properties of the crater, as observed for changes of lava lake levels or conduit geometry (i.e. Spina et al., 2019; Watson et al., 2019; Johnson et al., 2018).

6. Conclusion

We present one year of seismic, infrasound and satellite-based thermal data to characterize volcanic processes at Earth's only active carbonatite volcano Oldoinyo Lengai. Although this volcano has extensively been studied due to its unusual lavas, this is the first study concerned with geophysical signals of carbonatite eruptions. Seismic tremor is a ubiquitous phenomenon with a wide variety of signals, duration, frequencies and harmonic properties. We use RSAM to describe the strength of seismic tremor and detect significant changes throughout the year which often correspond to changes in the acoustic wavefield and thermal anomalies. We interpret that these changes are caused by a common volcano physical process. We define different activity styles which partially alternate throughout the year: intrusive activity, degassing, bubble bursting in a lava pond, hornito building and varying levels of extrusive activity, in particular spattering. Our findings

suggest the existence of a connected, shallow plumbing system within the crater floor which supplies hornitos and a lava pond with melt. Further, we observe significant changes in the dynamics of this system which, together with the overall elevated activity following previous years before our study, calls for permanent monitoring of this peculiar volcano, particularly multi-disciplinary approaches from geophysics to gas measurements. Our study emphasizes the importance of future experiments on volcanoes outside the realm of well-studied specimens. Further, laboratory and modeling work are necessary to characterize the relationship between the properties of seismo-acoustic tremor, the geological setting, the viscosity of the erupting lava as well as crater geometries.

Author contributions

M.C.R. is the PI of the SEISVOL project, processed the seismic and infrasound data, composed Figs. 1–9 and 11–13, and wrote the majority of the first draft of the manuscript. F.M. and A.C. processed the satellite data and wrote the sections on thermal data processing and observations. F.M composed Fig. 10. G.R. and A.S.L. installed the co-located seismic and infrasound stations. M.C.R., A.S.L., and G.R. acquired the field data, with substantial support by E.O.K. All authors contributed to the interpretation of the results and writing of the paper.

Funding

M.C.R is funded by the DFG (German Research Council), grant number RE 4321/1-1.

Declaration of Competing Interest

None.

Data availability

The dataset is archived at GEOFON Data Center, https://doi.org/10.14470/4W7564850022.

Acknowledgements

We highly appreciate everyone involved with the fieldwork, especially members of Engaresero Village. We thank the Tanzania Commission for Science and Technology (COSTECH) for supporting us and providing the research permits. The equipment for the seismic station was kindly provided by the Geophysical Instrument Pool Potsdam (GIPP) and the Goethe-University Frankfurt. Funding for the infrasound station was provided through Goethe-University Frankfurt research grants to G.R. Data were archived by GEOFON (GEOFON Data Centre, 1993). This manuscript benefitted from discussions with Editor Diana Roman and remarks by two anonymous reviewers.

Appendix A. Supplementary data

Supplementary data to this article can be found online at https://doi.org/10.1016/j.jvolgeores.2023.107898.

References

Aki, K., Koyanagi, R., 1981. Deep volcanic tremor and magma ascent mechanism under Kilauea, Hawaii. J. Geophys. Res. 86 (B8), 7095–7109. https://doi.org/10.1029/JB086iB08p07095.

Aki, K., Fehler, M., Das, S., 1977. Source mechanism of volcanic tremor: fluid driven crack models and their application to the 1963 Kilauea eruption. J. Volcanol. Geotherm. Res. 2, 259–287. https://doi.org/10.1016/0377-0273(77)90003-8.

Albaric, J., Perrot, J., Deverchere, J., Deschamps, A., Le Gall, B., Ferdinand, R.W., Petit, C., Tiberi, C., Sue, C., Songo, M., 2010. Contrasted seismogenic and rheological behaviours from shallow and deep earthquake sequences in the North Tanzanian Divergence, East Africa. J. Afr. Earth Sci. 58, 799–811.

Albaric, J., Deverchere, J., Perrot, J., Jakovlev, A., Deschamps, A., 2014. Deep crustal earthquakes in North Tanzania, East Africa: Interplay between tectonic and magmatic processes in an incipient rift. Geochem. Geophys. Geosyst. 15, 374–394. https://doi.org/10.1002/2013GC005027.

Arámbula-Mendoza, R., Valdés-González, C., Varley, N., Reyes-Pimentel, T.A., Juárez-García, B., 2016. Tremor and its duration-amplitude distribution at Popocatépetl volcano, Mexico. Geophys. Res. Lett. 43, 8994–9001. https://doi.org/10.1002/2016GL070227.

Baer, G., Hamiel, Y., Shamir, G., Nof, R., 2008. Evolution of a magma driven earthquake swarm and triggering of the nearby Oldoinyo Lengai eruption, as resolved by InSAR'a, ground observations and elastic modeling, East African Rift, 2007, Earth planet. Sci. Lett. 272, 339–352. https://doi.org/10.1016/j.epsl.2008.04.052.

Barrière, J., d'Oreye, N., Oth, A., Geirsson, H., Mashagiro, N., Johnson, J.B., Smets, B., Samsonov, S., Kervyn, F., 2018. Single-station seismo-acoustic monitoring of Nyiragongo's Lava Lake Activity (D.R. Congo). Front. Earth Sci. 6, 82. https://doi.org/10.3389/feart.2018.00082.

Battaglia, J., Aki, K., Staudacher, T., 2005. Location of tremor sources and estimation of lava output using tremor source amplitude on the Piton de la Fournaise volcano: 2. Estimation of lava output. J. Volcanol. Geotherm. Res. 147 (3–4), 291–308. https://doi.org/10.1016/j.jvolgeores.2005.04.006.

Benoit, J.P., Mcnutt, S.R., 1997. New constraints on source processes of volcanic tremor at Arenal Volcano, Costa Rica, using broadband seismic data. Geophys. Res. Lett. 24 (4), 449–452.

Biggs, J., Anthony, E.Y., Ebinger, C.J., 2009. Multiple inflation and deflation events at Kenyan volcanoes, East African Rift. Geology 37 (11), 979–982. https://doi.org/10.1130/G30133A.1.

Biggs, J., Chivers, M., Hutchinson, M.C., 2013. Surface deformation and stress interactions during the 2007–2010 sequence of earthquake, dyke intrusion and eruption in northern Tanzania. Geophys. J. Int. 195 (1), 16–26. https://doi.org/10.1093/gji/ggt226.

Calais, E., d'Oreye, N., Albaric, J., Deschamps, A., Delvaux, D., Déverchere, J., Ebinger, C., Ferdinand, R.W., Kervyn, F., Macheyeke, A.S., Oyen, A., Perrot, J., Saria, E., Smets, B., Stamps, D.S., Wauthier, C., 2008. Strain accommodation by slow slip and dyking in a youthful continental rift, East Africa. Nature 456 (7223), 783–787. https://doi.org/10.1038/nature07478.

Campus, A., Laiolo, M., Massimetti, F., Coppola, D., 2022. The transition from MODIS to VIIRS for global volcano thermal monitoring. Sensors 22, 1713. https://doi.org/10.3390/s22051713.

Cannata, A., Di Grazia, G., Montalto, P., Ferrari, F., Nunnari, G., Patanè, D., Privitera, E., 2010. New insights into banded tremor from the 2008–2009 Mount Etna eruption. J. Geophys. Res. 115, B12318. https://doi.org/10.1029/2009JB007120.

Cannata, A., Montalto, P., Patane, D., 2013. Joint analysis of infrasound and seismic signals by cross wavelet transform: detection of Mt. Etna explosive activity. Nat. Hazards Earth Syst. Sci. 13, 1669–1677. https://doi.org/10.5194/nhess-13-1669-2013.

Chouet, B., 1983. Ground motion near an expanding preexisting crack. J. Volcanol. Geotherm. Res. 19, 367–379. https://doi.org/10.1016/0377-0273(83)90119-1.

Chouet, B., 1988. Resonance of a fluid-driven crack: radiation properties and implications for the source of long-period events and harmonic tremor. J. Geophys. Res. 93, 4375–4400. https://doi.org/10.1029/JB093iB05p04375.

Chouet, B.A., Matoza, R.S., 2013. A multi-decadal view of seismic methods for detecting precursors of magma movement and eruption. J. Volcanol. Geotherm. Res. 252, 108–175. https://doi.org/10.1016/j.jvolg eores.2012.11013.

Coppola, D., Laiolo, M., Cigolini, C., Massimetti, F., Delle Donne, D., Ripepe, M., Arias, H., et al., 2020. Thermal Remote Sensing for Global Volcano Monitoring: Experiences From the MIROVA System. Front. Earth Sci. 7, 362. https://doi.org/10.3389/feart.2019.00362.

Coppola, D., Piscopo, D., Staudacher, T., Cigolini, C., 2009. Lava discharge rate and effusive pattern at Piton de la Fournaise from MODIS data. J. Volcanol. Geotherm. Res. 184 (1–2), 174–192. https://doi.org/10.1016/j.jvolgeores.2008.11.031.

Coppola, D., Laiolo, M., Cigolini, C., Donne, D.D., Ripepe, M., 2016. Enhanced volcanic hot-spot detection using MODIS IR data: results from the MIROVA system. Geol. Soc. Lond. Spec. Publ. 426, 181–205. https://doi.org/10.1144/sp426.5.

Coppola, D., Valade, S., Masias, P., et al., 2022. Shallow magma convection evidenced by excess degassing and thermal radiation during the dome-forming Sabancaya eruption (2012−2020). Bull. Volcanol. 84, 16. https://doi.org/10.1007/s00445-022-01523-1.

Daud, N., Stamps, D.S., Battaglia, M., Huang, M., Saria, E., Ji, K., 2023. Elucidating the magma plumbing system of Ol Doinyo Lengai (Natron Rift, Tanzania) using satellite geodesy and numerical modeling. J. Volcanol. Geotherm. Res. 438 https://doi.org/10.1016/j.jvolgeores.2023.107821.

Dawson, J.B., 1992. Neogene tectonics and volcanicity in the North Tanzania sector of the Gregory Rift Valley: contrasts with the Kenya sector. Tectonophysics 204, 81–83.

Dawson, J.B., Keller, J., Nyamweru, C., 1995. Historic and recent eruptive activity of Oldoinyo Lengai. In: Bell, K., Keller, J. (Eds.), Carbonatite Volcanism: Oldoinyo Lengai and the Petrogenesis of Natrocarbonatites, IAVCEI Proc Volcanol 4. Springer, Berlin, pp. 4–22.

Eibl, E.P.S., Bean, C.J., Jónsdóttir, I., Höskuldsson, A., Thordarson, T., Coppola, D., Witt, T., Walter, T.R., 2017. Multiple coincident eruptive seismic tremor sources during the 2014–2015 eruption at Holuhraun, Iceland. J. Geophys. Res. Solid Earth 122, 2972–2987. https://doi.org/10.1002/2016JB013892.

Endo, E.T., Murray, T., 1991. Real-time seismic amplitude measurement (RSAM): a volcano monitoring and prediction tool. Bull. Volcanol. 53 (7), 533–545. https://doi.org/10.1007/BF00298154.

Fee, D., Matoza, R.S., 2013. An overview of volcano infrasound: from Hawaiian to Plinian, local to global. J. Volcanol. Geotherm. Res. 249, 123–139. https://doi.org/10.1016/j.jvolgeores.2012.09.002.

Fee, D., Garcés, M., Patrick, M., Chouet, B., Dawson, P., Swanson, D., 2010. Infrasonic harmonic tremor and degassing bursts from Halema'uma'u Crater, Kilauea Volcano. Hawaii J. Geophys. Res. Solid Earth 115 (11), 1–15. https://doi.org/10.1029/2010JB007642.

Fischer, T.P., Morrissey, M.M., Lucia Calvache, V.M., Diego Gomez, M., Roberto Torres, C., Stix, J., Williams, S.N., 1994. Correlations between SO2 flux and long-period seismicity at Galeras volcano. Nature 368 (6467), 135–137.

Fischer, T.P., Burnard, P., Marty, B., Hilton, D.R., Furi, E., Palhol, F., Sharp, Z.D., Mangasini, F., 2009. Upper-mantle volatile chemistry at Oldoinyo Lengai volcano and the origin of carbonatites. Nature 459, 77–80. https://doi.org/10.1038/nature07977.

Foley, S.F., Link, K., Tiberindwa, J.V., Barifaijo, E., 2012. Patterns and origin of igneous activity around the Tanzanian craton. J. Afr. Earth Sci. 62 (1), 1–18. https://doi.org/10.1016/j.jafrearsci.2011.10.001.

Gestrich, J.E., Fee, D., Matoza, R.S., Lyons, J.J., Dietterich, H.R., Cigala, V., Kueppers, U., Patrick, M.R., Parcheta, C.E., 2022. Lava fountain jet noise during the 2018 eruption of fissure 8 of Kīlauea volcano. Front. Earth Sci. 10, 1027408. https://doi.org/10.3389/feart.2022.1027408.

Girona, T., Caudron, C., Huber, C., 2019. Origin of shallow volcanic tremor: the dynamics of gas pockets trapped beneath thin permeable media. J. Geophys. Res. Solid Earth 124, 4831–4861. https://doi.org/10.1029/2019JB017482.

Global Volcanism Program, 2019. Report on Ol Doinyo Lengai (Tanzania). In: Bennis, K. L., Venzke, E. (Eds.), Bulletin of the Global Volcanism Network, 47:8. Smithsonian Institution.

Harris, A., 2013. Thermal Remote Sensing of Active Volcanoes: A User's Manual, 432. Cambridge university press, Cambridge, MA. https://doi.org/10.1017/CBO9781139029346.

Hellweg, M., 2000. Physical models for the source of Lascar's harmonic tremor. J. Volcanol. Geotherm. Res. 101, 183–198. https://doi.org/10.1016/S0377-0273(00)00163-3.

Hotovec, A.J., Prejean, S.G., Vidale, J.E., Gomberg, J., 2013. Strongly gliding harmonic tremor during the 2009 eruption of Redoubt volcano. J. Volcanol. Geotherm. Res. 259, 89–99.

Ichihara, M., Yamakawa, K., Muramatsu, D., 2021. A simple method to evaluate the air-to-ground coupling efficiency: a tool helping the assessment of seismic/infrasonic energy partitioning during an eruption. Earth Planets Space 73, 180. https://doi.org/10.1186/s40623- 021-01510-4.

Johnson, J.B., 2003. Generation and propagation of infrasonic airwaves from volcanic explosions. J. Volcanol. Geotherm. Res. 121 (1), 1–14. https://doi.org/10.1016/S0377-0273(02)00408-0.

Johnson, J.B., Ripepe, M., 2011. Volcano infrasound: a review. J. Volcanol. Geotherm. Res. 206 (3–4), 61–69. https://doi.org/10.1016/j.jvolgeores.2011.06.006.

Johnson, J.B., Watson, L.M., Palma, J.L., Dunham, E.M., Anderson, J.F., 2018. Forecasting the eruption of an open-vent volcano using resonant infrasound tones. Geophys. Res. Lett. 45, 2213–2220. https://doi.org/10.1002/2017GL076506.

Jolly, A., Kennedy, B., Edwards, M., Jousset, P., Scheu, B., 2016. Infrasound tremor from bubble burst eruptions in the viscous shallow crater lake of White Island, New Zealand, and its implications for interpreting volcanic source processes. J. Volcanol. Geotherm. Res. 327, 585–603. https://doi.org/10.1016/j.jvolgeores.2016.08.010.

Julian, B.R., 1994. Volcanic tremor: Nonlinear excitation by fluid flow. J. Geophys. Res. 99 (B6), 11,859–11,877. https://doi.org/10.1029/93JB03129.

Keller, J., Klaudius, J., Kervyn, M., Ernst, G.G.J., Mattsson, H.B., 2010. Fundamental changes in the activity of the natrocarbonatite volcano Oldoinyo Lengai, Tanzania. Bull.Volcanol. 72, 893–912. https://doi.org/10.1007/s00445-010-0371-x.

Kervyn, M., Ernst, G.G.J., Klaudius, J., et al., 2008. Voluminous lava flows at Oldoinyo Lengai in 2006: chronology of events and insights into the shallow magmatic system. Bull. Volcanol. 70, 1069–1086. https://doi.org/10.1007/s00445-007-0190-x.

Kervyn, M., Ernst, G.G.J., Keller, J., Vaughan, G., Klaudius, J., Pradal, E., Belton, F., Mattsson, H., Mbede, E., Jacobs, P., 2010. Fundamental changes in the activity of the natrocarbonatite volcano Oldoinyo Lengai, Tanzania. II. Eruptive behavior. Bull. Volcanol. https://doi.org/10.1007/s00445-010-0360-0.

Klaudius, J., Keller, J., 2006. Peralkaline silicate lavas at Oldoinyo Lengai, Tanzania. Lithos 91, 173–190. https://doi.org/10.1016/j.lithos.2006.03.017.

Konstantinou, K.I., Schlindwein, V., 2002. Nature, wavefield properties and source mechanism of volcanic tremor: a review. J. Volcanol. Geotherm. Res. 119 (1–4), 161–187. https://doi.org/10.1016/S0377-0273(02)00311-6.

Koulakov, I., Shapiro, N., 2021. Seismic tomography of volcanoes. In: Encyclopedia of Earthquake Engineering, vol. d. Springer Berlin Heidelberg, pp. 1–18. https://doi.org/10.1007/978-3-642-36197-5_51-1.

Laiolo, M., Ripepe, M., Cigolini, C., Coppola, D., Della Schiava, M., Genco, R., Innocenti, L., Lacanna, G., Marchetti, E., Massimetti, F., Silengo, M.C., 2019. Space- and ground-based geophysical data tracking of magma migration in shallow feeding system of Mount Etna Volcano. Remote Sens. 11, 1182. https://doi.org/10.3390/rs11101182.

Krafft, M., Keller, J., 1989. Temperature meas- urements in carbonatite lava lakes and flows, Oldoinyo Lengai, Tanzania. Science 245, 168–170.

Laiolo, M., Donne, D.D., Coppola, D., Bitetto, M., Cigolini, C., Schiava, M.D., Innocenti, L., et al., 2022. Shallow magma dynamics at open-vent volcanoes tracked by coupled thermal and SO2 observations. Earth Planet. Sci. Lett. 594 https://doi.org/10.1016/j.epsl.2022.117726.

Le Gall, B., Nonnotte, P., Rolet, J., Benoit, M., Guillou, H., Mousseau-Nonnotte, M., Albaric, J., Deverchere, J., 2008. Rift propagation at craton margin. Distribution of faulting and volcanism in the North Tanzanian Divergence (East Africa) during Neogene times. Tectonophysics 448, 1–19. https://doi.org/10.1016/j.tecto.2007.11.005.

Mana, S., Furman, T., Turrin, B.D., Feigenson, M.D., Swisher, C.C., 2015. Magmatic activity across the East African North Tanzanian Divergence Zone. J. Geol. Soc. 172, 368. https://doi.org/10.1144/jgs2014-072.

Massimetti, F., Coppola, D., Laiolo, M., Valade, S., Cigolini, C., Ripepe, M., 2020. Volcanic hot-spot detection using SENTINEL-2: a comparison with MODIS–MIROVA thermal data series. Remote Sens. 12, 820.

Matoza, R.S., Fee, D., 2014. Infrasonic component of volcano-seismic eruption tremor. Geophys. Res. Lett. 41, 1964–1970. https://doi.org/10.1002/2014GL059301.

Matoza, R., Roman, D., 2022. One hundred years of advances in volcano seismology and acoustics. Bull. Volcanol. 84, 86. https://doi.org/10.1007/s00445-022-01586-0.

Matoza, R., Fee, D., Garcés, M., 2010. Infrasonic tremor wavefield of the Pu'u ‘O¯ ‘o¯ crater complex and lava tube system, Hawaii, in April 2007. J. Geophys. Res. 115 (B12312) https://doi.org/10.1029/2009JB007192.

McKee, K., Fee, D., Haney, M., Matoza, R.S., Lyons, J., 2018. Infrasound signal detection and back azimuth estimation using ground-coupled airwaves on a seismo-acoustic sensor pair. J. Geophys. Res. Solid Earth 123, 6826–6844. https://doi.org/10.1029/2017JB015132.

McNutt, S.R., 1992. Volcanic tremor. In: Nierenberg, W.A. (Ed.), Encyclopedia of Earth System Science 4. Academic Press, San Diego, pp. 417–425.

McNutt, S.R., 1996. Seismic monitoring and eruption forecasting of volcanoes: A review of the state-of-the-art and case histories. In: Scarpa, Tilling (Ed.), Monitoring and Mitigation of Volcanic Hazards. Springer, Berlin, pp. 100–146.

Mollex, G., Füri, E., Burnard, P., Zimmermann, L., Chazot, G., Kazimoto, E.O., Marty, B., France, L., 2018. Tracing helium isotope compositions from mantle source to fumaroles at Oldoinyo Lengai volcano, Tanzania. Chem. Geol. 480, 66–74. https://doi.org/10.1016/j.chemgeo.2017.08.015.

Muirhead, J.D., Kattenhorn, S.A., Le Corvec, N., 2015. Varying styles of magmatic strain accommodation across the East African Rift. Geochem. Geophys. Geosyst. 16, 2. https://doi.org/10.1002/2015gc005918.

Muirhead, J.D., Kattenhorn, S.A., Lee, H., Mana, S., Turrin, B.D., Fischer, T.P., Stamps, D. S., 2016. Evolution of upper crustal faulting assisted by magmatic volatile release during early-stage continental rift development in the East African Rift. Geosphere 12 (6), 1670–1700. https://doi.org/10.1130/ges01375.1.

Muirhead, J.D., Fischer, T.P., Oliva, S.J., Laizer, A., van Wijk, J., Currie, C.A., Takahata, N., 2020. Displaced cratonic mantle concentrates deep carbon during continental rifting. Nature 582 (7810), 67–72. https://doi.org/10.1038/s41586-020-2328-3.

Neuberg, J., Luckett, R., Baptie, B., Olsen, K., 2000. Models of tremor and low-frequency earthquake swarms on Montserrat. J. Volcanol. Geotherm. Res. 101, 83–104. https://doi.org/10.1016/S0377-0273(00)00169-4.

Oliva, S.J., Ebinger, C.J., Wauthier, C., Muirhead, J.D., Roecker, S.W., Rivalta, E., Heimann, S., 2019. Insights into fault-magma interactions in an early-stage continental rift from source mechanisms and correlated volcano-tectonic earthquakes. Geophys. Res. Lett. 46 (4), 2065–2074. https://doi.org/10.1029/2018gl080866.

Oppenheimer, C., Rothery, D.A., Francis, P.W., 1993. Thermal distributions at fumarole fields - implications for infrared remote-sensing of active volcanos. J. Volcanol. Geotherm. Res. 55 (1–2) https://doi.org/10.1016/0377-0273(93)90092-6, 490 97–115.

Picard, D., 1985. Testing and estimating change-points in time series. Adv. Appl. Probab. 17 (4), 841–867. https://doi.org/10.2307/1427090.

Reath, K., Pritchard, M., Poland, M., Delgado, F., Carn, S., Coppola, D., et al., 2019. Thermal, 515 deformation, and degassing remote sensing time series (CE 2000–2017) at the 47 most active 516 volcanoes in Latin America: Implications for volcanic systems. J. Geophys. Res. Solid Earth 124, 195–218. https://doi.org/10.1029/2018JB016199.

Reiss, M.C., Rümpker, G., 2020. SEISVOL - Seismic and Infrasound Networks to Study the Volcano Oldoinyo Lengai. GFZ Data Services. 10.14470/4W7564850022.

Reiss, M.C., Muirhead, J.D., Laizer, A.S., Link, F., Kazimoto, E.O., Ebinger, C.J., Rümpker, G., 2021. The impact of complex volcanic plumbing on the nature of Seismicity in the developing Magmatic Natron Rift, Tanzania. Front. Earth Sci. 8, 609805 https://doi.org/10.3389/feart.2020.609805.

Reiss, M.C., De Siena, L., Muirhead, J.D., 2022. The Interconnected magmatic plumbing system of the Natron rift. Geophys. Res. Lett. 49 (15), e2022GL098922 https://doi.org/10.1029/2022gl098922.

Ripepe, M., Poggi, P., Braun, T., Gordeev, E., 1996. Infrasonic waves and volcanic tremor at Stromboli. Geophys. Res. Lett. 23, 181–184. https://doi.org/10.1029/95GL03662.

Ripepe, M., Delle Donne, D., Lacanna, G., Marchetti, E., Ulivieri, G., 2009. The onset of the 2007 Stromboli effusive eruption recorded by an integrated geophysical network. J. Volcanol. Geotherm. Res. 182 (3–4), 131–136. https://doi.org/10.1016/j.jvolgeores.2009.02.011.

Ripepe, M., Marchetti, E., Bonadonna, C., Harris, A.J.L., Pioli, L., Ulivieri, G., 2010. Monochromatic infrasonic tremor driven by persistent degassing and convection at Villarrica Volcano. Chile. Geophys. Res. Lett. 37 (15), 2–7. https://doi.org/10.1029/2010GL043516.

Roecker, S., Ebinger, C., Tiberi, C., Mulibo, G., Wambura, F., Mtelela, K., Kianji, G., Muzuka, A., Gautier, S., Albaric, J., Peyrat, S., 2017. Subsurface images of the Eastern Rift, Africa, from the joint inversion of body waves, surface waves and gravity: investigating the role of fluids in early-stage continental rifting. Geophys. J. Int. 210 (2), 931–950. https://doi.org/10.1093/gji/ggx220.

Roman, D.C., 2017. Automated detection and characterization of harmonic tremor in continuous seismic data. Geophys. Res. Lett. 44 https://doi.org/10.1002/2017GL073715.

Rosenblatt, B.B., Johnson, J.B., Anderson, J.F., et al., 2022. Controls on the frequency content of near-source infrasound at open-vent volcanoes: a case study from Volcán Villarrica, Chile. Bull. Volcanol. 84, 103. https://doi.org/10.1007/s00445-022-01607-y.

Sciotto, M., Watson, L.M., Cannata, A., et al., 2022. Infrasonic gliding reflects a rising magma column at Mount Etna (Italy). Sci. Rep. 12, 16954. https://doi.org/10.1038/s41598-022-20258-9.

Sherrod, D.R., Magigita, M.M., Kwelwa, S., 2013. Geologic map of Oldonyo Lengai (Oldoinyo Lengai) and surroundings, Arusha Region, United Republic of Tanzania, U.S. Geol. Surv. Rep. 2013–1306, p. 65.

Shevchenko, A.V., Dvigalo, V.N., Zorn, E.U., Vassileva, M.S., Massimetti, F., Walter, T.R., Svirid, I.Y., Chirkov, S.A., Ozerov, A.Y., Tsvetkov, V.A., Borisov, I.A., 2021. Constructive and destructive processes during the 2018–2019 eruption episode at Shiveluch Volcano, Kamchatka, studied from satellite and aerial data. Front. Earth Sci. 9. https://www.frontiersin.org/articles/10.3389/feart.2021.680051.

Spina, L., Cannata, A., Morgavi, D., 2019. Degassing behaviour at basaltic volcanoes: New insights from experimental investigations of different conduit geometry and magma viscosity. Earth Sci. Rev. https://doi.org/10.1016/j.earscirev.2019.03.010.

Stamps, D.S., Saria, E., Ji, K.H., Jones, J.R., Ntambila, D., Daniels, M.D., Mencin, D., 2016. Real-time data from the Tanzania Volcano Observatory at the Ol Doinyo Lengai volcano in Tanzania (TZVOLCANO). UCAR/NCAR-EarthCube. https://doi.org/10.5065/D6P849BM.

Tournigand, P., Smets, B., Laxton, K., Dille, A., France, L., Chazot, G., Wauthier, C., Nicholson, E.J., Kasanzux, C., Msechux, M., Kervyn, M., 2023. Remote Volcano Monitoring Using Crowd-Sourced Imagery and SfM-MVS Photogrammetry: The Case Study of Oldoinyo Lengai Pit Crater since the 2007–08 Paroxysm (Submitted to JVGR).

Unglert, K., Jellinek, A.M., 2015. Volcanic tremor and frequency gliding during dike intrusions at K¯ılauea—a tale of three eruptions. J. Geophys. Res. Solid Earth 120, 1142–1158. https://doi.org/10.1002/2014JB011596.

Valade, S., Lacanna, G., Coppola, D., et al., 2016. Tracking dynamics of magma migration in open-conduit systems. Bull. Volcanol. 78, 78. https://doi.org/10.1007/s00445-016-1072-x.

Vaughan, R.G., Kervyn, M., Realmuto, V., Abrams, M., Hook, S.J., 2008. Satellite measurements of recent volcanic activity at Oldoinyo Lengai, Tanzania. J. Volcanol. Geotherm. Res. 173 (3–4), 196–206. https://doi.org/10.1016/j.jvolgeores.2008.01.028.

Watson, L.M., Dunham, E.M., Johnson, J.B., 2019. Simulation and inversion of harmonic infrasound from open-vent volcanoes using an efficient quasi-1D crater model. J. Volcanol. Geotherm. Res. 380 (2019), 64–79. https://doi.org/10.1016/j.jvolgeores.2019.05.007.

Weinstein, A., Oliva, S.J., Ebinger, C.J., Roecker, S., Tiberi, C., 2017. Fault-magma interactions during early continental rifting: Seismicity of the Magadi-Natron-Manyara basins, Africa. Geochem. Geophys. Geosyst. https://doi.org/10.1002/2017GC007027.

Wilding, J.D., Zhu, W., Ross, Z.E., Jackson, J.M., 2023. The magmatic web beneath Hawai'i. Science 379, 462–468. https://doi.org/10.1126/science.ade5755.

Wooster, M.J., Zhukov, B., Oertel, D., 2003. Fire radiative energy for quantitative study of biomass burning: derivation from the BIRD experimental satellite and comparison to MODIS fire products. Remote Sens. Environ. 86 (1), 83–107. ISSN 0034–4257. https://doi.org/10.1016/S0034-4257(03)00070-1.

Wright, R., Flynn, L., Garbeil, H., Harris, A., Pilger, E., 2002. Automated volcanic eruption detection using MODIS. Remote Sens. Environ. 82 (1), 135–155. ISSN 0034–4257. https://doi.org/10.1016/S0034-4257(02)00030-5.